Pulsar timing array signals induced by black hole binaries in relativistic eccentric orbits

Abhimanyu Susobhanan[*] and Achamveedu Gopakumar
Department of Astronomy and Astrophysics, Tata Institute of Fundamental Research, Mumbai 400005, Maharashtra, India

George Hobbs
CSIRO Astronomy and Space Science, Australia Telescope National Facility, Box 76, Epping, NSW 1710, Australia

Stephen R. Taylor
Department of Physics & Astronomy, Vanderbilt University, 2301 Vanderbilt Place, Nashville, Tennessee 37235, USA

(Received 23 November 2019; accepted 7 February 2020; published 27 February 2020)

Individual supermassive black hole binaries in noncircular orbits are possible nanohertz gravitational wave sources for the rapidly maturing Pulsar Timing Array experiments. We develop an accurate and efficient approach to compute Pulsar Timing Array signals due to gravitational waves from inspiraling supermassive black hole binaries in relativistic eccentric orbits. Our approach employs a Keplerian-type parametric solution to model third post-Newtonian accurate precessing eccentric orbits while a novel semianalytic prescription is provided to model the effects of quadrupolar order gravitational wave emission. These inputs lead to a semianalytic prescription to model such signals, induced by nonspinning black hole binaries inspiraling along arbitrary eccentricity orbits. Additionally, we provide a fully analytic prescription to model Pulsar Timing Array signals from black hole binaries inspiraling along moderately eccentric orbits, influenced by Boetzel *et al.* [Phys. Rev. D **96**, 044011 (2017)]. These approaches are being incorporated into Enterprise and TEMPO2 for searching the presence of such binaries in Pulsar Timing Array datasets.

DOI: 10.1103/PhysRevD.101.043022

I. INTRODUCTION

Pulsar Timing Array (PTA) experiments are expected to inaugurate the field of nanohertz gravitational wave (GW) astronomy during the next decade [1]. This will augment the ground-based GW astronomy, established by the LIGO Scientific Collaboration and the Virgo collaboration during the present decade, operating mainly in the hectohertz to kilohertz frequency regime [2]. A PTA experiment monitors an ensemble of millisecond pulsars (MSPs) to search for correlated deviations to their pulse times of arrival (TOAs) to infer the presence of GWs [3]. These efforts are sensitive to long-wavelength (∼1 nHz–100 nHz) GWs, where the lower and upper limits of the frequency range are, respectively, set by the total span and cadence of the PTA observations [4]. Therefore, PTAs are expected to detect GWs from supermassive black hole (SMBH) binaries with milliparsec orbital separations [5]. At present, there exist three matured PTA efforts, namely the Parkes Pulsar Timing Array (PPTA) [6], the European Pulsar Timing Array (EPTA) [7], and the North American Nanohertz Observatory for Gravitational Waves (NANOGrav) [8,9]. Additionally, there are emerging PTA efforts from India, China, and South Africa [10–12]. The International Pulsar Timing Array (IPTA) consortium combines data and resources to achieve more quickly the first detection of nanohertz GWs [13–15].

There are a number of promising astrophysical and cosmological GW sources in the nanohertz frequency window [16,17]. We expect the first detected signal to be the ensemble of GWs from many SMBH binaries, producing a stochastic GW background (SGWB). This should be followed by the detection of bright individual SMBH binaries that resound above this background [18,19]. Stringent observational constraints are being placed on both types of PTA sources due to the absence of any firm detections in the PTA datasets [20–25]. In the case of SMBH binaries in circular orbits, the present sky-averaged upper limit on GW strain is below 7.3×10^{-15} at 8 nHz [21].

---

[*] s.abhimanyu@tifr.res.in

Such constraints on SMBH binaries can be invoked to restrict their astrophysical formation and evolution scenarios [26–30]. It will be desirable to extend the above bounds to eccentric binaries since SMBH binaries emitting nanohertz GWs can have non-negligible orbital eccentricities [17]. It was noted that SMBH binaries originating from gas-rich galaxy mergers may have non-negligible eccentricities even during their late inspiral phase [31,32]. Additionally, realistic N-body simulations of massive galaxy mergers result in SMBH binaries in eccentric orbits due to stellar interactions [33–36]. Therefore, it will be interesting to probe the presence of such binaries in the existing PTA datasets. This demands general relativistic constructs that can be implemented in the popular pulsar timing software packages like TEMPO2 and Enterprise [37–39].

In the present paper, we develop an accurate and efficient prescription to obtain PTA signals induced by isolated SMBH binaries inspiraling along general relativistic eccentric orbits. Our approach employs the post-Newtonian (PN) approximation which allows us to model black holes (BHs) as point particles [40]. Recall that PN approximation provides general relativistic corrections to Newtonian dynamics in powers of $(v/c)^2 \sim GM/c^2 r$, where v, M, and r are, respectively, the relative velocity, total mass, and relative separation of a BH binary. We let BH binaries move in 3PN-accurate precessing eccentric orbits with the help of generalized quasi-Keplerian parametrization [41], where the 3PN-accurate description incorporates $(\frac{v}{c})^6$-order general relativistic corrections to Newtonian motion. Additionally, we incorporate the effects of GW emission at the dominant quadrupolar order with the help of a GW phasing formalism, detailed in Refs. [42,43], while adapting recent results from Ref. [44]. This allows us to model PTA signals due to nonspinning SMBH binaries inspiraling along 3PN-accurate eccentric orbits in a semianalytic manner. The numerical treatments are required only to solve the PN-accurate Kepler equation and to integrate the resulting fractional pulsar frequency shift induced by passing GWs. These considerations ensure that the prescription is general relativistically accurate and computationally efficient. It turns out that the PN description is quite appropriate to model such PTA signals as the SMBH binaries are expected to merge at orbital frequencies outside the PTA frequency window [17]. Additionally, we provide a fully analytic prescription to compute PTA signals induced by isolated SMBH binaries inspiraling along moderately eccentric orbits. This result heavily depends on a fully analytic approach to compute temporally evolving GW polarization states for compact binaries moving in PN-accurate moderately eccentric orbits [45]. We note in passing that the present effort extends and improves efforts to compute PTA signals due to GWs from compact binaries inspiraling along Newtonian accurate eccentric orbits [46,47].

In what follows, we list below the salient features of the present paper.

(i) A brief description of our approach for computing quadrupolar-order PTA signals due to inspiral GWs from nonspinning massive BH binaries in PN-accurate precessing eccentric orbits while employing the PN-accurate Keplerian-type parametric solution and the GW phasing approach of Ref. [42] is presented in Sec. II A and Sec. II B.

(ii) An accurate and computationally efficient way to incorporate the effects of GW emission on the parametrized conservative PN-accurate orbital dynamics and its salient features are presented in Sec. II C. This subsection explains why we require a one-time numerical solution of a differential equation to incorporate the effects of quadrupolar GW emission in our approach. Plots displaying PTA signals that arise from our semianalytical approach and their various facets are provided in Sec. II D. The computational costs associated with our modeling of the PTA signals, induced by GWs from massive BH binaries in PN-accurate arbitrary eccentricity orbits are provided in Sec. II E.

(iii) A fully analytic way of computing PTA signals for moderate eccentricities ($e \lesssim 0.3$) is presented in Sec. III where we employed crucial inputs from Ref. [45]. This approach provides a powerful check on our detailed semianalytic prescription, and this is demonstrated by comparing PTA signals computed using our semianalytic and fully analytic methods in the low-eccentricity regime.

In brief, we developed an accurate and efficient prescription to compute PTA signals induced by isolated SMBH binaries inspiraling along general relativistic eccentric orbits, employing for the first time an accurate semianalytic solution to describe PN-accurate orbital evolution of BH binaries. An implementation of the PTA signals derived in this work is available at https://github.com/abhisrkckl/GWecc.

II. PTA SIGNALS FROM BH BINARIES IN QUASI-KEPLERIAN ECCENTRIC ORBITS

We begin by deriving expressions for the dominant quadrupolar order $+/\times$ residuals in Sec. II A. How we describe temporal evolution of various dynamical variables that appear in these expressions is described in Sec. II B and Sec. II C, which is followed by a pictorial exploration of our main results in Sec. II D and an exploration of the associated computational costs in Sec. II E. The present paper explores the effects of far-zone GWs on the pulsar TOAs, and this is realistic as our GW sources are extragalactic while the pulsars exist within our Galaxy.

A. Timing residual expressions at the dominant quadrupolar order

When a GW signal passes across the line of sight between a pulsar and the observer along a direction $\hat{n}$, it perturbs the underlying space-time metric. This induces temporally evolving changes in the measured pulsar rotational frequency ν [48]

$$\frac{\Delta\nu(t_E)}{\nu} \equiv z_{\rm GW}(t_E) = h(t_E) - h(t_P), \tag{1}$$

where h stands for the dimensionless GW strain, t_E and t_P denote, respectively, the instances when a GW passes the solar system barycenter (SSB) and the pulsar, and the rotational frequency ν is measured in the SSB frame. These two time instances differ by the usual geometric delay such that

$$t_P = t_E - \frac{D_P}{c}(1 + \hat{n}\cdot\hat{p}) = t_E - \frac{D_P}{c}(1 - \cos\mu), \tag{2}$$

where D_P is the distance to the pulsar while $\hat{p}$ specifies its direction with respect to the SSB, and μ provides the angle between $\hat{n}$ and $\hat{p}$. Influenced by Ref. [49], the GW strain h can be written in terms of the two GW polarization states $h_{+,\times}$ as

$$h(t) = [F_+ \quad F_\times]\begin{bmatrix}\cos 2\psi & -\sin 2\psi\\ \sin 2\psi & \cos 2\psi\end{bmatrix}\begin{bmatrix}h_+(t)\\ h_\times(t)\end{bmatrix}, \tag{3}$$

where $F_{+,\times}$ are the antenna pattern functions that depend on the sky locations of the pulsar and the GW source, and ψ is the polarization angle of the GW. The explicit expressions for $F_{+,\times}$ involve angles that specify the directions $\hat{n}$ and $\hat{p}$ [namely, the right ascension (RA) and declination (DEC) of the GW source and the pulsar], and are available in Ref. [50].

The temporally evolving GW-induced redshift causes differences between the expected and the observed TOAs of pulses. This is given by

$$R(t_E) = \int_0^{t_E} z_{\rm GW}(t')dt' = s(t_E) - s(t_P), \tag{4}$$

where $s(t)$ is given by

$$s(t) = \int_0^t h(t')dt' = F_+ s_+(t) + F_\times s_\times(t), \tag{5}$$

and we have defined

$$s_{+,\times}(t) = \int_0^t h_{+,\times}(t')dt'. \tag{6}$$

This quantity $R(t_E)$ is usually referred to as the GW-induced (prefit) pulsar timing residual or the PTA signal, and is essentially prescribed by the values of $s_{+,\times}$ at the SSB and the pulsar positions. It is customary to refer to $s(t_E)$ and $s(t_P)$ as the Earth and pulsar terms, and $s_{+,\times}$ as the plus/cross residuals, respectively.

The leading quadrupolar order $h_{+,\times}$ expressions for a nonspinning eccentric binary, available in Ref. [45], read

$$h_+^Q = \frac{GM\eta}{D_L c^2} x \frac{1}{(1-\chi)^2}\Big(-2(c_i^2+1)\sqrt{1-e_t^2}\xi\sin(2\phi) + (c_i^2+1)(2e_t^2 - \chi^2 + \chi - 2)\cos(2\phi) + s_i^2(1-\chi)\chi\Big), \tag{7a}$$

$$h_\times^Q = \frac{GM\eta}{D_L c^2} x \frac{1}{(1-\chi)^2} 2c_i\Big(2\sqrt{1-e_t^2}\xi\cos(2\phi) + (2e_t^2 - \chi^2 + \chi - 2)\sin(2\phi)\Big), \tag{7b}$$

where ϕ denotes the angular coordinate in the orbital plane, called the orbital phase [see Eqs. (9b) and (14) below for the definition of ϕ for Newtonian and PN-accurate orbits] while the superscript Q indicates the quadrupolar order contributions to $h_{+,\times}$. The total mass, symmetric mass ratio and luminosity distance to the binary are represented by $M = m_1 + m_2$, $\eta = \frac{m_1 m_2}{M^2}$, and D_L, respectively. Further, we use shorthand notations to denote trigonometric functions of the orbital inclination i, namely $c_i = \cos i$ and $s_i = \sin i$, while $\chi = e_t \cos u$ and $\xi = e_t \sin u$, where u is the eccentric anomaly. The orbital eccentricity is specified by e_t and it is associated with the PN-accurate Kepler equation [41]. The dimensionless PN parameter $x = (GMn/c^3)^{2/3}$ employs the mean motion n associated with the Kepler equation, which is related to the orbital period P_b by $n = 2\pi/P_b$. In addition, the polarization angle ψ present in Eq. (3) provides a measure of the longitude of the ascending node in the case of nonspinning binaries.

To obtain Eqs. (7), we begin from the quadrupolar order $h_{+,\times}$ expressions that are valid for compact binaries in noncircular orbits [42]

$$h_+^Q(r,\phi,\dot{r},\dot{\phi}) = -\frac{GM\eta}{D_L c^4}\left[(1+c_i^2)\left[\left(\frac{GM}{r} + r^2\dot{\phi}^2 - \dot{r}^2\right)\cos 2\phi + 2r\dot{r}\dot{\phi}\sin 2\phi\right] + s_i^2\left(\frac{GM}{r} - r^2\dot{\phi}^2 - \dot{r}^2\right)\right], \tag{8a}$$

$$h_\times^Q(r,\phi,\dot{r},\dot{\phi}) = -\frac{GM\eta}{D_L c^4} 2c_i\left[\left(\frac{GM}{r} + r^2\dot{\phi}^2 - \dot{r}^2\right)\sin 2\phi - 2r\dot{r}\dot{\phi}\cos 2\phi\right], \tag{8b}$$

where r and ϕ provide the radial and angular coordinates that specify the position of the reduced mass m_1m_2/M around the total mass M in the center of mass frame of the binary, while $\dot{r} = dr/dt$ and $\dot{\phi} = d\phi/dt$. We employ the Keplerian parametric solution for eccentric orbits to provide parametric expressions for these dynamical variables. The classical Keplerian parametric solution, neatly summarized in Ref. [51], provides the following parametric expressions for r and ϕ:

$$r = a(1 - e\cos u), \tag{9a}$$

$$\phi - \phi_0 = f, \tag{9b}$$

where a and e specify, respectively, the orbital semimajor axis and the Newtonian orbital eccentricity such that $0 \leq e < 1$, while ϕ_0 is some initial orbital phase. The true anomaly f is related to the eccentric anomaly u by the relation

$$f = 2\arctan\left[\left(\frac{1+e}{1-e}\right)^{1/2}\tan\frac{u}{2}\right]. \tag{10}$$

This approach provides temporal evolution for r and ϕ in a semianalytic manner as u is related to the coordinate time t by the transcendental Kepler equation [51]

$$l \equiv n(t - t_0) = u - e\sin u, \tag{11}$$

where l is called the mean anomaly and t_0 denotes the epoch of periapsis passage.

With the help of the such a parametric solution, it is fairly easy to obtain expressions for r, $\dot{r}$, and $\dot{\phi}$ in terms of u, e and x. This essentially leads to Eqs. (7) from Eqs. (8) for $h^{Q}_{+,\times}$. Note that we need an accurate and efficient method to tackle the above transcendental Eq. (11) to obtain the actual temporal evolution for the two polarization states. We note in passing that Eqs. (7) and (8) are also invoked to obtain inspiral templates for stellar mass compact binaries in eccentric binaries [52,53].

In the next subsection, we summarize our approach to provide fully 3PN-accurate temporal evolution for our $h^{Q}_{+,\times}$ expressions.

B. Accurate description for the evolution of nonspinning BH binaries inspiraling along precessing eccentric orbits

We begin by outlining our approach to describe the orbital evolution of nonspinning BH binaries inspiraling along 3PN-accurate quasi-Keplerian eccentric orbits. This prescription is crucial to specify how the angular variables (ϕ, u) and the orbital elements (n, e_t) vary in time while computing $R(t)$ as evident from Eqs. (7). First, we adapt the GW phasing formalism, detailed in Refs. [42,43], for computing temporally evolving $h_{+,\times}(t)$. This approach involves splitting the orbital dynamics of compact binaries into certain conservative and reactive parts. In the PN terminology, the conservative dynamics usually provides PN corrections that are even powers of (v/c), while reactive dynamics involves odd powers of (v/c) beginning with $\mathcal{O}((v/c)^5)$ contributions. Such a split is justified as the reactive effects due to GW emission first enter the orbital dynamics only at the $(v/c)^5$ (2.5PN) order and act in timescales much longer than the orbital period when the binary is not close to its merger. This split also allows us to employ a PN-accurate Keplerian-type parametric solution for describing the 3PN-accurate conservative orbital dynamics, detailed in Ref. [41]. Extending Eq. (9b) to 3PN order, we write the 3PN-accurate orbital phase as

$$\phi - \phi_0 = (1 + k)l + W(u(l), n, e_t), \tag{12}$$

where the angular variable $W(u)$ is 2π periodic in u, and k represents the advance of periapsis per orbit [42,43]. We do not display here the explicit 3PN-accurate expressions for k and $W(u)$ in terms of n, e_t, M, and η. However, these expressions in the modified harmonic gauge are available as Eqs. (11b) and (25a–25h) in Ref. [43]. Clearly, we need to specify how u varies with time to obtain 3PN-accurate temporal orbital phase evolution. The following 3PN-accurate Kepler Equation, which extends Eq. (11), provides the required ingredient

$$l = u - e_t\sin u + \mathfrak{F}_t(u), \tag{13}$$

where the explicit 3PN-accurate expression for $\mathfrak{F}_t(u)$ in terms of u, n, e_t, M, and η is given by Eq. (27) in Ref. [43]. It is helpful to solve the above equation by invoking an improved version of Mikkola's method to obtain 3PN-accurate temporal phase evolution [52]. Recall that Mikkola's method provides the most accurate and efficient method to solve the classical Kepler Equation and determine $u(l)$ [54]. For the present effort, it is rather convenient to rewrite the above expression for the orbital phase as

$$\phi = l + \gamma + (1 + k)(f - l) + \mathfrak{F}_\phi(u), \tag{14}$$

where $\gamma - \gamma_0 = kn(t - t_0)$ tracks the evolution of the periapsis, and the true anomaly f is given by

$$f = 2\arctan\left[\left(\frac{1+e_\phi}{1-e_\phi}\right)^{1/2}\tan\frac{u}{2}\right], \tag{15}$$

where e_ϕ is some angular eccentricity such that $0 \leq e_\phi < 1$. The explicit 3PN-accurate expression for e_ϕ in terms of e_t, n, M and η is available in Ref. [42]. We note that the angular variable γ is not identical to the argument of periapsis ω, usually defined for Keplerian orbits as $\phi - \omega = f$. This angular variable is termed as the angle of periapsis and evolves as $\gamma - \gamma_0 = kn(t - t_0)$ for conservative PN orbits. Further, the definition of the mean anomaly l, namely $l = n(t - t_0)$, ensures that both l and γ are linear-in-time varying angular variables. Note that the use of Eqs. (13) and (14) in our expressions for $h^Q_{+,\times}$, given by Eqs. (7), leads to an essentially analytic way for modeling temporally evolving quadrupolar GW polarization states. The resulting waveforms are displayed as the dashed line plots in Fig. 1 and we clearly see the periapsis advance-induced amplitude modulations in moderate to high eccentricity plots. It is important to note that these dashed line plots provide $h^Q_{+,\times}$ associated with compact binaries moving in *conservative* 3PN-accurate precessing eccentric orbits.

Clearly, we need a prescription to include the effects of GW emission to model $h_{+,\times}(t)$ for compact binaries inspiraling along PN-accurate eccentric orbits. This is pursued by adapting the GW phasing formalism of Refs. [42,43]. This formalism demonstrated that GW emission forces n and e_t to change with time and it is possible to split their temporal evolution into two parts [42]. The first part leads to the secular or orbital-averaged evolution equations for n and e_t which ensure that both n and e_t can change substantially over the gravitational radiation reaction timescale. The second part essentially provides periodic variations to n and e_t in the orbital timescale, which remain tiny during the early inspiral phase of compact binary evolution [42]. Therefore, we ignore such periodic variations to n and e_t for the present investigation as our focus is indeed on the early part of the BH binary inspiral. The secular evolution of n and e_t ensures that l and γ no longer follow linear-in-time variations as noted earlier. With the inclusion of gravitation

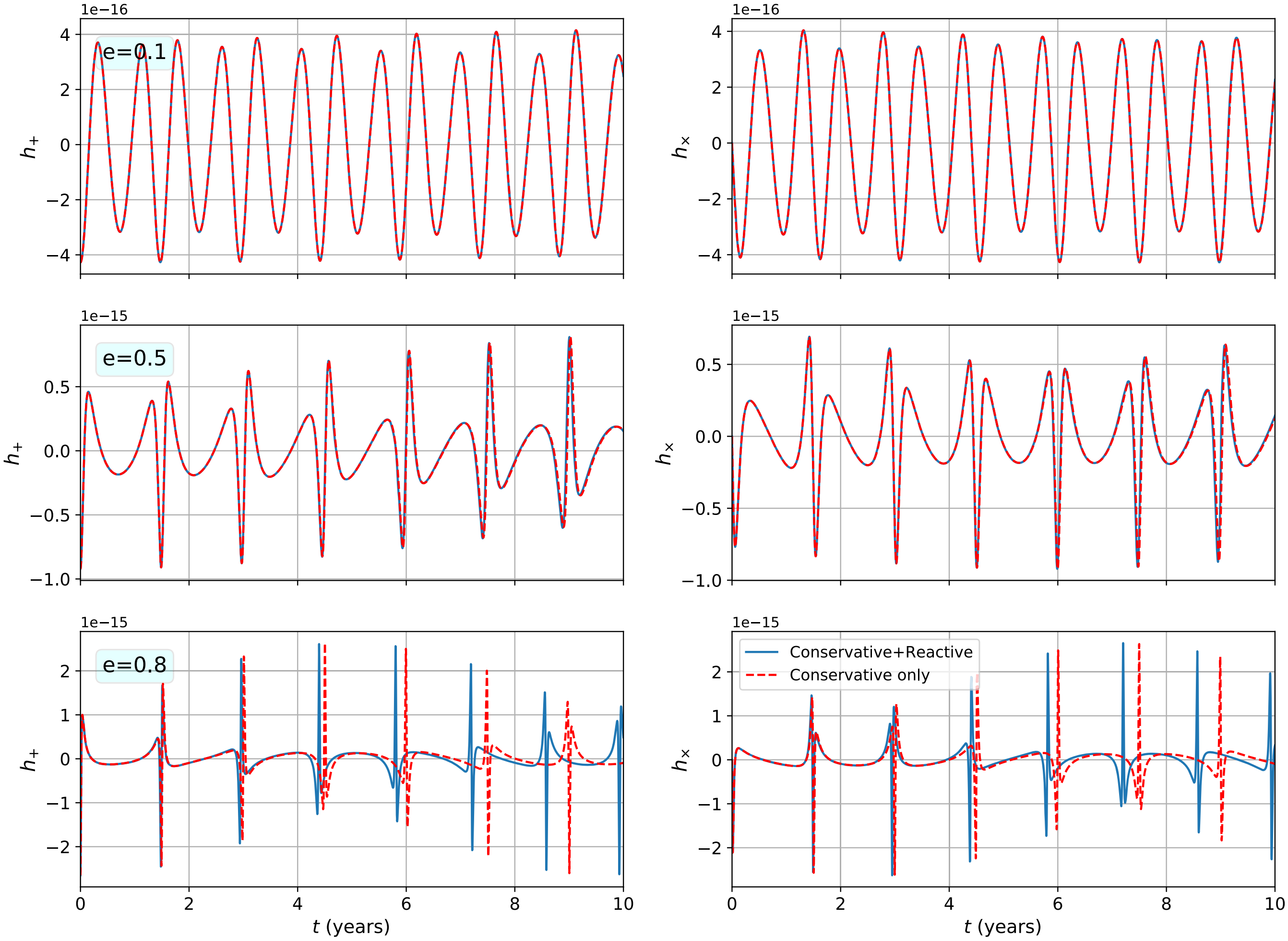

FIG. 1. Temporally evolving $h^Q_{+,\times}$, namely quadrupolar order GW polarization states, associated with massive BH binaries in 3PN-accurate eccentric orbits. The solid line plots incorporate the effects of GW emission that enter the binary BH dynamics at the 2.5PN order and we ignore the effects of gravitational radiation reaction in the dashed line plots. We let $M = 10^9 M_\odot$, $\eta = 0.25$, $D_L = 1$ Gpc, $P_b = 1.5$ years, $i = 0$ and $\psi = 0$ while selecting three e_t values (the listed e_t values provide orbital eccentricities at $t_E = 0$ epoch in all our figures). The periapsis advance-induced amplitude modulations are clearly visible in the plots for moderately high to high eccentric binaries while GW emission-induced *chirping* is apparent in the $e = 0.8$ plots.

radiation reaction effects, the explicit temporal evolution for l and γ becomes

$$l - l_0 = \int_{t_0}^{t} n(t')\, dt', \tag{16a}$$

$$\gamma - \gamma_0 = \int_{t_0}^{t} k(t') n(t')\, dt', \tag{16b}$$

where we have ignored orbital timescale variations in these angular variables [42]. These considerations imply that the GW phasing formalism provides a set of coupled differential equations for n, e_t, γ, and l. The resulting set of *four* coupled ordinary differential equations (ODEs) that incorporate secular effects of quadrupolar order GW emission read [42],

$$\frac{dn}{dt} = \frac{1}{5}\left(\frac{GM_{\mathrm{ch}} n}{c^3}\right)^{\frac{5}{3}} n^2 \frac{(96 + 292 e_t^2 + 37 e_t^4)}{(1 - e_t^2)^{7/2}}, \tag{17a}$$

$$\frac{de_t}{dt} = \frac{-1}{15}\left(\frac{GM_{\mathrm{ch}} n}{c^3}\right)^{\frac{5}{3}} n e_t \frac{(304 + 121 e_t^2)}{(1 - e_t^2)^{5/2}}, \tag{17b}$$

$$\frac{d\gamma}{dt} = kn, \tag{17c}$$

$$\frac{dl}{dt} = n, \tag{17d}$$

where $M_{\mathrm{ch}} = \eta^{3/5} M$ is the chirp mass of the binary. Note that we are required to solve the above set of four differential equations along with 3PN-accurate expressions for u and ϕ, given by Eqs. (13) and (14) to describe the orbital phase evolution of compact binaries inspiraling along 3PN-accurate eccentric orbits. In the next subsection, we develop a method to tackle these coupled differential equations in an essentially semianalytic way.

C. Semianalytic description for $n(t)$, $e_t(t)$, $\gamma(t)$, and $l(t)$

We begin by describing our computationally efficient way to obtain $n(t)$ and $e_t(t)$, influenced by Refs. [42,44]. Our approach involves deriving certain analytic expressions for $n(e_t)$ and $t(e_t)$ and appropriately treating them numerically to obtain an accurate and efficient way to track the temporal evolution in $n(t)$ and $e_t(t)$. To obtain an analytic expression for $n(e_t)$, we divide Eq. (17a) by Eq. (17b), and this leads to

$$\frac{dn}{de_t} = -3 \frac{n}{e_t} \frac{1}{(1 - e_t^2)} \frac{(96 + 292 e_t^2 + 37 e_t^4)}{(304 + 121 e_t^2)}. \tag{18}$$

It is easy to integrate the above equation to obtain

$$n(e_t) = n_0 \left(\frac{e_{t0}}{e_t}\right)^{\frac{18}{19}} \left(\frac{1 - e_t^2}{1 - e_{t0}^2}\right)^{\frac{3}{2}} \left(\frac{304 + 121 e_{t0}^2}{304 + 121 e_t^2}\right)^{\frac{1305}{2299}}, \tag{19}$$

where n_0 and e_{t0} are the values of n and e_t at some initial epoch $t = t_0$ [42]. Unfortunately, it is not easy to obtain such a compact expression for $e_t(t)$. To obtain an equation that can be analytically tackled, we substitute the above equation for $n(e_t)$ in Eq. (17b). The resulting equation may be written as

$$\frac{de_t}{dt} = -\kappa \frac{(1 - e_t^2)^{3/2}}{e_t^{29/19} (121 e_t^2 + 304)^{1181/2299}}, \tag{20a}$$

where

$$\kappa = \frac{1}{15}\left(\frac{GM_{\mathrm{ch}} n_0}{c^3}\right)^{\frac{5}{3}} \frac{n_0 e_{t0}^{\frac{48}{19}} (121 e_{t0}^2 + 304)^{\frac{3480}{2299}}}{(1 - e_{t0}^2)^4}. \tag{20b}$$

Note that the coefficient κ is only a function of certain intrinsic binary BH parameters like the chirp mass, initial values of the mean motion and orbital eccentricity. Further, it is not difficult to infer that κ has the dimensions of frequency and is nonzero for eccentric binaries. These considerations influenced us to introduce a dimensionless temporal parameter τ such that $\tau = \tau_0 - \kappa(t - t_0)$, and Eq. (20a) in terms of τ becomes

$$\frac{de_t}{d\tau} = \frac{(1 - e_t^2)^{3/2}}{e_t^{29/19} (121 e_t^2 + 304)^{1181/2299}}, \tag{21}$$

and we will clarify the significance of the constant τ_0 later. Interestingly, this equation does not contain any intrinsic (and constant) binary BH parameters. In other words, the above equation is valid for all eccentric compact binaries while restricting the GW emission effects to the leading quadrupolar order. It turns out that it is possible to obtain an analytical solution for Eq. (21), as noted in Ref. [44], and it reads

$$\tau(e) = \frac{e^{\frac{48}{19}}}{768} \mathrm{F}_1^{\mathrm{A}}\left(\frac{24}{19}; \frac{-1181}{2299}, \frac{3}{2}; \frac{43}{19}; \frac{-121 e^2}{304}, e^2\right), \tag{22}$$

where $\mathrm{F}_1^{\mathrm{A}}$ represents Appell's 2D hypergeometric function [55], and we have chosen the initial condition $\tau(0) = 0$ so that the constant of integration vanishes. It is indeed computationally very expensive to invert the above expression to get $e_t(\tau)$, mainly due to the difficulty in computing $\mathrm{F}_1^{\mathrm{A}}$ numerically. Therefore, we precompute $e_t(\tau)$ at a sufficiently dense set of points and interpolate between those points to get $e_t(\tau)$ for arbitrary values of τ. Such a *look-up table* of $e_t(\tau)$ may be obtained either by numerically solving Eq. (21) or by inverting Eq. (22). The resulting $e_t(\tau)$ plot is displayed in Fig. 2 and it is important to note that GW emission forces e_t to advance from right to

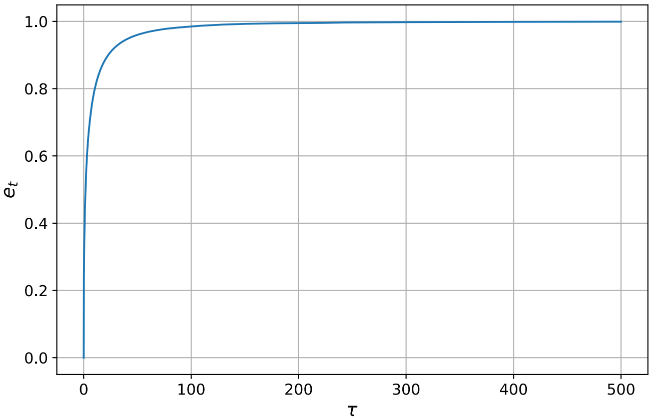

FIG. 2. Numerical solution of Eq. (21) that provides $e_t(\tau)$. Note that the dimensionless temporal variable τ is defined as $\tau \equiv \tau_0 - \kappa(t - t_0)$ and this is why a compact binary evolves from right to left along the τ axis. Let us emphasize that this curve defines the orbital eccentricity evolution for all compact binaries and the origin provides certain Newtonian merger epoch.

left in our $e_t(\tau)$ plot. This is essentially due to the way τ is related to the coordinate time t, namely $\tau = \tau_0 - \kappa(t - t_0)$. We have verified that our $e_t(\tau)$ evolution is consistent with Eq. (51) of Ref. [44].

We note here that the frequency $n \to \infty$ as $e_t \to 0$ as evident from Eq. (19) and it influenced us to define certain merger time *in our 2.5PN approximation* as the instant when $e_t \to 0$. We are now in a position to explain the meaning of τ_0 and, for this purpose, we define certain dimensionless merger time by invoking the initial condition $\tau(0) = 0$. This allows us to specify the above undetermined constant as $\tau_0 = \tau(e_{t0})$, where $\tau(e_t)$ is given by Eq. (22). We identify τ_0 as certain dimensionless merger time because it is possible to compute certain "Newtonian" merger time for compact binaries with its help. The relevant expression for such a merger time is given by

$$t^{2.5\mathrm{PN}}_{\mathrm{merg}} = \frac{\tau_0}{\kappa}, \tag{23}$$

and we have verified that this expression, in the small eccentricity limit, is indeed consistent with Eq. (50) of Ref. [56]. Recall that Ref. [56] computed the "Newtonian merger time" for compact binaries that incorporates the leading order eccentricity contributions as

$$\lim_{e_0 \to 0} t^{2.5\mathrm{PN}}_{\mathrm{merg}} \sim \frac{5}{n_0}\left(\frac{GM_{\mathrm{ch}} n_0}{c^3}\right)^{-\frac{5}{3}}\left(\frac{1}{256} - \frac{157 e_0^2}{11008}\right). \tag{24}$$

Additionally, we have computed an equivalent expression for such a merger time in the Appendix B while clarifying our way to treat the $\kappa \to 0$ scenario.

Note that as a binary BH approaches the $\tau = 0$ epoch, its orbital dynamics becomes more relativistic and this eventually leads to the breakdown of the present quadrupolar (or 2.5PN) order description of the binary BH reactive dynamics. Therefore, our prescription should only be used for an observational duration $t - t_0$ which is substantially smaller than $t^{2.5\mathrm{PN}}_{\mathrm{merge}}$. It turns out that our fully 3PN-accurate orbital description that incorporates the effects of quadrupolar order GW emission is quite appropriate while dealing with the expected isolated SMBH binary PTA sources.

We now turn our attention to the evolution equations for γ and l, given by Eqs. (17c) and (17d). The plan is to express both n and kn in terms of e_t, n_0 and e_0 with the help of our $n(e_t)$ expression. Further, we employ our τ variable rather than its coordinate time (t) counterpart. This leads to

$$\frac{dl}{d\tau} = -\alpha \frac{(1 - e_t^2)^{\frac{3}{2}}}{e_t^{\frac{18}{19}}(304 + 121 e_t^2)^{\frac{1305}{2299}}}, \tag{25a}$$

$$\frac{d\gamma}{d\tau} = -\beta \frac{(1 - e_t^2)^{\frac{3}{2}}}{e_t^{\frac{30}{19}}(304 + 121 e_t^2)^{\frac{2175}{2299}}}, \tag{25b}$$

where the dimensionless coefficients α and β are given by

$$\alpha = \left(\frac{GM_{\mathrm{ch}} n_0}{c^3}\right)^{-\frac{5}{3}} \frac{15(1 - e_{t0}^2)^{5/2}}{e_{t0}^{\frac{30}{19}}(121 e_{t0}^2 + 304)^{\frac{2175}{2299}}}, \tag{26a}$$

$$\beta = \left(\frac{GM_{\mathrm{ch}} n_0}{c^3}\right)^{-\frac{5}{3}} \left(\frac{GM n_0}{c^3}\right)^{\frac{2}{3}} \frac{45(1 - e_{t0}^2)^{3/2}}{e_{t0}^{\frac{18}{19}}(121 e_{t0}^2 + 304)^{\frac{1305}{2299}}}. \tag{26b}$$

It should be noted that we have only used the dominant order contributions to k, namely $k = 3x/(1 - e_t^2)$, while obtaining the above equation for $d\gamma/dt$. Its 3PN extension is provided in Appendix A.

The next step is to obtain differential equations for l and γ that are independent of binary BH intrinsic (and constant) parameters. To this end, we define two scaled and shifted variables $\bar{l} = L_0 - l/\alpha$ and $\bar{\gamma} = \Gamma_0 - \gamma/\beta$. Invoking Eqs. (25a) and (25b), it is fairly straightforward to obtain the following differential equations for $\bar{l}$ and $\bar{\gamma}$

$$\frac{d\bar{l}}{d\tau} = \frac{(1 - e_t^2)^{\frac{3}{2}}}{e_t^{\frac{18}{19}}(304 + 121 e_t^2)^{\frac{1305}{2299}}}, \tag{27a}$$

$$\frac{d\bar{\gamma}}{d\tau} = \frac{(1 - e_t^2)^{\frac{3}{2}}}{e_t^{\frac{30}{19}}(304 + 121 e_t^2)^{\frac{2175}{2299}}}, \tag{27b}$$

with the following initial conditions $l(\tau_0) = l_0$ and $\gamma(\tau_0) = \gamma_0$. These initial conditions imply that the shifts L_0 and Γ_0 are given by

$$L_0 = \bar{l}(\tau_0) + \frac{l_0}{\alpha}, \tag{28a}$$

$$\Gamma_0 = \bar{\gamma}(\tau_0) + \frac{\gamma_0}{\beta}. \tag{28b}$$

The structure of the above two differential equations support analytic solutions if we compute the $d\bar{l}/de_t$ and $d\bar{\gamma}/de_t$ versions of Eqs. (27a) and (27b) with the help of Eq. (21) for $de_t/d\tau$. This results in

$$\frac{d\bar{l}}{de_t} = \frac{e_t^{11/19}}{(121e_t^2 + 304)^{124/2299}}, \tag{29a}$$

$$\frac{d\bar{\gamma}}{de_t} = \frac{e_t^{-1/19}}{(121e_t^2 + 304)^{994/2299}}. \tag{29b}$$

The fact that the rhs of these equations depend only on e_t allows us to obtain the following expressions for $\bar{l}$ and $\bar{\gamma}$:

$$\bar{l}(e_t) = \frac{19^{\frac{2175}{2299}}}{30 \times 2^{\frac{496}{2299}}} e_t^{\frac{30}{19}} {}_2\mathrm{F}_1\left(\frac{124}{2299}, \frac{15}{19}; \frac{34}{19}; \frac{-121e_t^2}{304}\right), \tag{30a}$$

$$\bar{\gamma}(e_t) = \frac{19^{\frac{1305}{2299}}}{36 \times 2^{\frac{1677}{2299}}} e_t^{\frac{18}{19}} {}_2\mathrm{F}_1\left(\frac{994}{2299}, \frac{9}{19}; \frac{28}{19}; \frac{-121e_t^2}{304}\right), \tag{30b}$$

where ${}_2\mathrm{F}_1$ is the Gaussian hypergeometric function, and we have verified that the above expression for $\bar{l}$ is consistent with Eq. (52) of Ref. [44]. In Fig. 3, we plot these variables against e_t and find the expected sharp rise in $\bar{l}$ for higher orbital eccentricities. It is important to note that these plots are independent of the intrinsic (and constant) binary BH parameters like the total mass, mass ratio, and initial orbital eccentricity and period.

To obtain the actual temporal evolution for the above set of variables, namely n, e_t, l and γ, we proceed as follows. First, we compute a look-up table for $e_t(\tau)$ by solving the differential equation for $de_t/d\tau$ as described earlier. We emphasize here that this is a one-time computation since the differential equation (21) does not contain any system-dependent parameters, which implies that the look-up table, once computed, may be saved and reused for later computations. (Details of this computation are given in subsection II C 1.) Thereafter, we determine $n(\tau)$, $l(\tau)$, and $\gamma(\tau)$ with the help of Eqs. (19), (30a), and (30b) that involve hypergeometric functions. Using the explicit expressions for τ_0, κ, α, and β and specific relations that connect τ to t, $\bar{l}$ to l, and $\bar{\gamma}$ to γ, it is straightforward to obtain binary BH system-dependent temporal evolution for n, e_t, l, and γ in terms of the regular coordinate time t. Let us emphasize that these variable changes are easy to implement as they essentially involve analytic expressions. To ascertain the accuracy of this procedure, we compared $n(t)$, $e_t(t)$, $\gamma(t)$ and $l(t)$ computed using this method to results obtained by numerically solving the system of ODEs (17) for different initial conditions, masses and mass ratios. We find that the results agree up to the numerical precision of the ODE solver as expected.

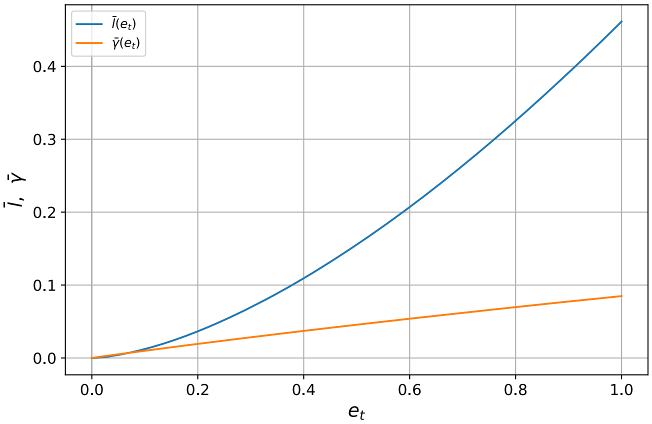

FIG. 3. The nonlinear variation of our two scaled angular variables $\bar{l}$ and $\bar{\gamma}$ as function of e_t. The use of these variables ensures that such variations are system independent at the quadrupolar order GW emission.

The variables u and ϕ which appear in the waveform (7) may be computed using Eqs. (13)–(14). Finally, the PTA signal $R(t)$ can be computed by numerically integrating the waveform as given by Eqs. (3)–(6). We are forced to perform this integral numerically owing to the fact that the waveform (7) is a function of u and ϕ which are not simple functions of the coordinate time.

1. Computation of $e_t(\tau)$

Clearly, an accurate and efficient prescription to obtain $e_t(\tau)$ is crucial for describing the temporal evolution of (n, e_t, γ, l) in terms of the coordinate time t. The fact that an explicit expression is available only for $\tau(e_t)$ and not for $e_t(\tau)$ forced us to obtain $e_t(\tau)$ either by numerically integrating Eq. (21) or by numerically inverting the analytic expression for $\tau(e_t)$ given by Eq. (22). However, we pursued the relatively computationally inexpensive approach of computing a look-up table for $e_t(\tau)$ at a sufficiently dense sample of τ values for one time. Thereafter, we obtain values of $e_t(\tau)$ at arbitrary τ values by interpolating between the precomputed values and this is heavily influenced by the universal nature of Eq. (21). In practice, we solve Eq. (21) using an adaptive ODE solver, which adjusts the step size to ensure an optimal accuracy of the solution while constructing the look-up table. This is important as the curvature of the function $e_t(\tau)$ is highly variable, as evident from Fig. (2). Therefore, the look-up table must be computed at a nonuniform sample of points such that the regions of high curvature are sampled at sufficiently high density for ensuring high accuracy.

This approach poses a new challenge since our $de_t/d\tau$ equation diverges at $e_t = 0$ as evident from Eq. (21). This implies that the numerical integration cannot start with the expected initial condition, namely $e_t(0) = 0$. We avoid this issue by starting the numerical integration at a small nonzero value of τ, say certain τ_{min}. To compute such an initial condition $e_t(\tau_{\mathrm{min}})$, we explore the asymptotic

$(\tau, e_t) \rightarrow (0,0)$ behavior of Eq. (21). In this limit, Eq. (21) becomes

$$\lim_{\tau, e_t \rightarrow 0} \frac{de_t}{d\tau} \sim \frac{1}{304^{\frac{1181}{2299}} e_t^{\frac{29}{19}}}, \tag{31}$$

where we have expanded the rhs of Eq. (21) to the leading order contributions in e_t. This equation can be integrated to obtain

$$\lim_{\tau \rightarrow 0} e_t(\tau) \sim \frac{2^{559/726} 3^{19/48}}{19^{145/242}} \tau^{19/48}. \tag{32}$$

Therefore, the new initial condition becomes

$$e_{t,\mathrm{min}} = \frac{2^{559/726} 3^{19/48}}{19^{145/242}} \tau_{\mathrm{min}}^{19/48}, \tag{33}$$

for some sufficiently small τ_{min}. The look-up table for $\tau(e)$ can now be computed by integrating Eq. (21) from τ_{min} to some τ_{max} such that it covers all eccentricity values of interest.

It is also possible to provide an estimate for τ_{max} where we can stop the numerical integration. Using the fact that $\lim_{\tau \rightarrow \infty} e_t = 1$, we write Eq. (21) in the $\tau \rightarrow \infty$ limit as

$$\lim_{\tau \rightarrow \infty} \frac{d\epsilon}{d\tau} \sim \frac{2\sqrt{2}\epsilon^{3/2}}{5\, 5^{63/2299} 17^{1181/2299}}, \tag{34}$$

where we have substituted $\epsilon = 1 - e_t$ in Eq. (21) and expanded the rhs of the resulting equation to the leading order in ϵ. This equation can be solved fairly easily to obtain

$$\lim_{\tau \rightarrow \infty} e_t \sim 1 - \frac{4}{(a\tau + b)^2}, \tag{35}$$

where we have defined the coefficient

$$a = \frac{2\sqrt{2}}{5 \times 5^{63/2299} 17^{1181/2299}}. \tag{36}$$

In contrast, the coefficient b may be computed by imposing the initial condition $e_t(\tau_{\mathrm{max}}) = e_{t,\mathrm{max}}$ to be

$$b = \frac{2}{\sqrt{1 - e_{t,\mathrm{max}}}} - a\tau_{\mathrm{max}}. \tag{37}$$

In our approach, we provide these limits to obtain an accurate and efficient prescription to evaluate $e_t(\tau)$.

We are now in a position to obtain the PTA signals due to massive BH binaries inspiraling along 3PN-accurate eccentric orbits, and this is what we explore in the next subsection.

D. Pictorial exploration of $R(t)$ due to BH binaries in relativistic eccentric orbits

We begin by displaying temporally evolving quadrupolar order $h^Q_{+,\times}(t)$, specified by Eqs. (7), while employing our semianalytic prescription for evolving n, e_t, γ, and l in Fig. 1. It should be noted that our explicit expressions for $h^Q_{+,\times}$ involve u and, therefore, we additionally need to invert the 3PN-accurate Kepler Equation, given by Eq. (13), at every l value to obtain the temporal evolution of our dominant order GW polarization states. The treatment of PN-accurate Kepler Equation, as noted earlier, is performed by adapting and extending the Mikkola's method [54,57]. The resulting $h_{+,\times}(t)$ associated with massive BH binaries inspiraling along fully 3PN-accurate eccentric orbits are displayed in Fig. 1, and are labelled "Conservative + Reactive". The effects of GW emission are clearly visible in $e = 0.8$ plots and it causes certain waveform dephasing while comparing with plots that do not include the effects of GW emission. Let us emphasize that our semianalytic approach is capable of treating orbital eccentricities that are ≤ 1 as we explicitly employ the eccentric anomaly u to trace the PN-accurate eccentric orbit.

We now have all the ingredients to obtain ready-to-use PTA signals associated with nonspinning SMBH binaries inspiraling along PN-accurate eccentric orbits. As mentioned earlier, the fact that $h^Q_{+,\times}$ expressions given by Eqs. (7) explicitly contain u and ϕ prevents us from evaluating analytically the integrals that appear in the expression for $R(t)$ as evident from Eqs. (4)–(6). Therefore, we employ an adaptive numerical integration routine, namely the QAG routine [58] to evaluate Eqs. (4)–(6) while computing pulsar timing residuals. We first provide a pictorial depiction of $R(t)$ and explain its various features with the help of $+/\times$ residual plots.

We display in Fig. 4 PTA signals induced on PSR J0437–4715 by a fiducial equal mass BH binary having $M = 10^9\ M_\odot$ with face-on orbit ($i = 0$) at a luminosity distance of 1 Gpc, for three different eccentricities and two different orbital periods. We let the sky location of the GW source to be RA $08^h 00^m 00^s$, DEC $-20°00'00''$, with $\psi = 0$. Each panel in Fig. 4 corresponds to a particular combination of orbital eccentricity and orbital period at the $t_E = 0$ epoch. Additionally, we choose two estimates for the pulsar distance, namely 156.79 pc and 157.04 pc, which are consistent with the 1σ uncertainty for its measurement, available in Ref. [59]. These choices lead to two plots each in six panels of Fig. 4. Amplitude modulations, visible in the moderate to high eccentricity cases for $P_b = 1.5$ yrs, are due to the fact that the pulsar term contributions can have substantially different orbital eccentricity and period for such high eccentric systems. Interestingly, temporal evolution of $R(t)$ is pulsar distance-dependent especially for the lower and moderate e values as evident from the first two panels for $P_b = 1.5$ yrs. Prominent dephasing in the

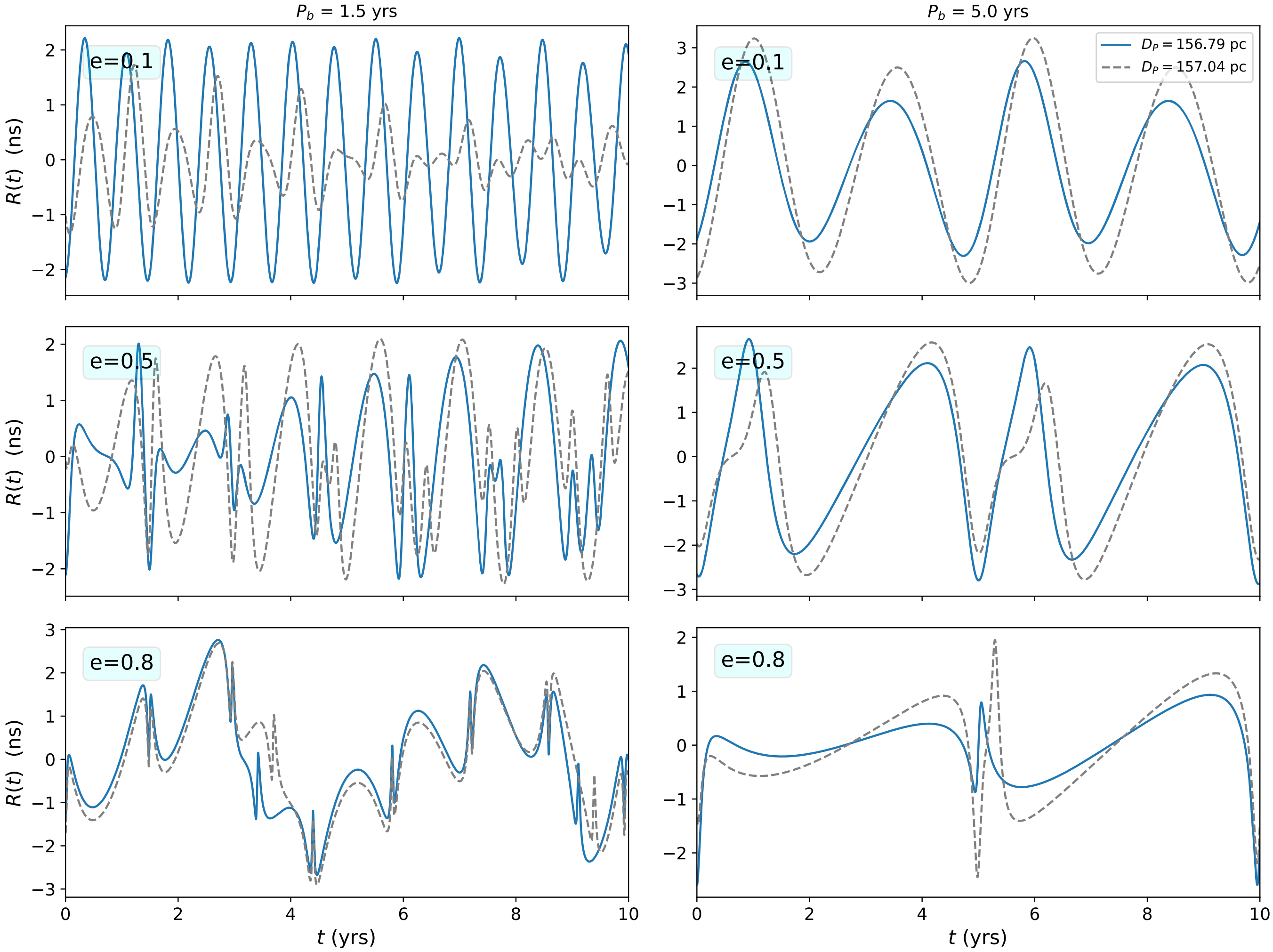

FIG. 4. PTA signals induced on PSR J0437–4715 by a fiducial massive BH binary at 1 Gpc away with two different P_b values and three e_t values at $t_E = 0$ epoch. The location of this pulsar is given by RA $04^h37^m16^s$, DEC $-47°15'09''$ and is at a distance of 156.79 pc [59]. The sky location of the binary is arbitrarily chosen to be RA $08^h00^m00^s$, DEC $-20°00'00''$ and other binary parameters are the same as in Fig. 5. The dashed plots correspond to a pulsar distance of 157.04 pc, which is off from the measured distance by its 1σ uncertainty [59]. It is very clear that the features of $R(t)$ for $P_b = 1.5$ yrs are very sensitive to the pulsar distance, especially for low and moderate eccentricities. This may be attributed to the frequencies of the Earth and pulsar terms being similar for low and moderate eccentricities and the pulsar distance difference being roughly equivalent to half the orbital period. In contrast, the features of the $P_b = 5$ yrs case are much less sensitive to the pulsar distance as the pulsar distance difference is not tuned to the orbital period.

$P_b = 1.5$ yrs case may be due to the fact that the change in pulsar distance is roughly equivalent to half of the orbital period. Such changes in the $R(t)$ evolution are less pronounced for the high e case as the underlying frequencies of the Earth and pulsar terms are significantly different. In contrast, such strong dependence of $R(t)$ on the pulsar distance is not observed in the $P_b = 5$ yrs case due to the fact that the pulsar distance difference is not tuned to the orbital period. Interestingly, the epochs of the sharp features, visible in Fig. 4, are very sensitive to the pulsar distance in the $P_b = 1.5$ yrs case, and its implications are being investigated.

To get a pulsar-independent view of these timing residuals, we plot in Fig. 5 the associated $+/\times$ residuals while separating the Earth and the Pulsar term contributions using identical parameters to Fig. 4, with $P_b = 5$ yrs. These plots confirm our earlier statement that the pulsar term, which provides a snapshot of the orbital configuration of our GW source at an earlier epoch, can have substantially different orbital eccentricity and period, especially for highly eccentric BH binaries. It is clearly the mixing of the two contributions with very different evolution timescales that produces various features present in our $R(t)$ plots.

We now proceed to display the quadrupolar nature of our PTA signal in Fig. 6. Specifically, we plot certain strength of the Earth term as a function of the sky location of the pulsar for a given GW source. This strength of the Earth

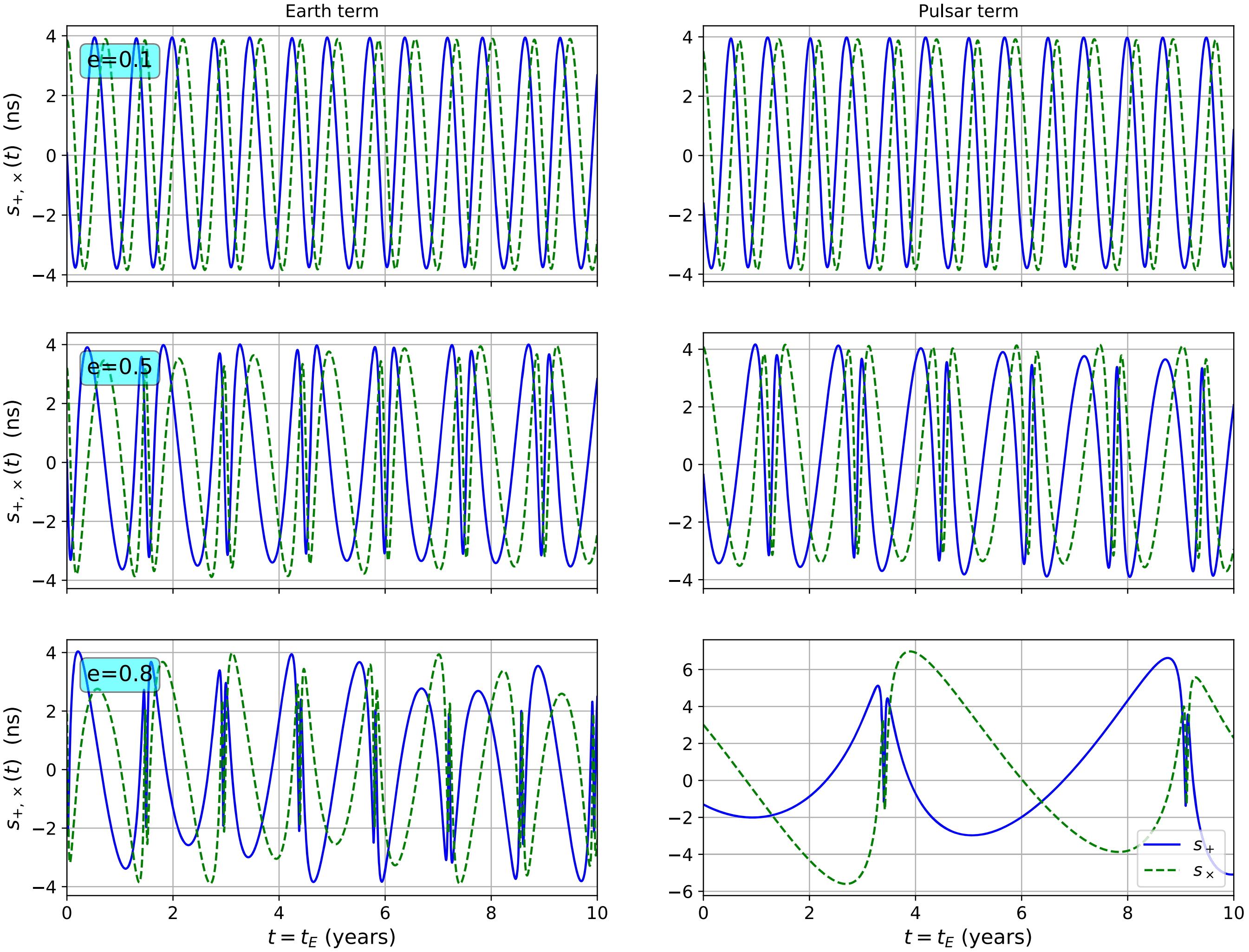

FIG. 5. Plots of $s_{+,\times}(t)$, namely the plus/cross residuals, for a 1 Gpc away equal mass binary BH having different orbital eccentricities at the initial Earth epoch while all other binary parameters are similar to those in Fig. 1 with $P_b = 1.5$ yrs at $t_E = 0$. We plot both the Earth and the Pulsar term contributions while assuming a geometric delay of 1000 years between these two locations. The GW emission ensures that fiducial pulsar contributions to $s_{+,\times}(t)$ have higher orbital eccentricities and periods. This is very prominent for the large initial eccentricity ($e = 0.8$) binary BH configuration.

term is defined as the difference between the maximum and minimum of $s(t_E)$ within a given time span. The top and bottom panels show such $s(t_E)$ strength for $\psi = 0$ and $\psi = 45°$ values, respectively. For these plots, we let the orbital eccentricity of the GW source to be 0.5 and the all other parameters are same as in Fig. 4 and Fig. 5. Our plots clearly show the quadrupolar pattern of the expected PTA signal, and the comparison between the top and bottom panels reveals the 45° rotation that is expected from the ψ values. Additionally, these plots essentially confirm that we are employing appropriate expressions for $F_\times$ and F_+.

We now turn our attention towards the numerical costs of our approach to obtain the temporal evolution of n, e_t, γ, and l as well as the computation of the PTA signal $R(t)$, and this is what we explore in the next subsection.

E. The cost of computing the orbital evolution and the PTA signal

We begin by comparing the computational cost of our semianalytic approach against numerically solving Eqs. (17) to obtain the orbital evolution. Excluding the one-time cost of computing the look-up table for $e(\tau)$, the execution time $t^{\rm exec}$ taken to compute the state of the orbit (n, e_t, γ, l) at a given set of TOAs should depend on the number of TOAs ($N_{\rm TOA}$) as well as their total observation span/integration span (specified by some t_0 and t_1). This is illustrated in the top panel of Fig. 7 where we plot the execution time per TOA ($t^{\rm exec}/N_{\rm TOA}$) required to compute our variables (n, e, γ, l) as a function of $N_{\rm TOA}$ for different integration spans $(t_1 - t_0)$ in our semianalytic approach. This panel shows that the computational time required for evaluating (n, e, γ, l) at a given TOA is independent of both

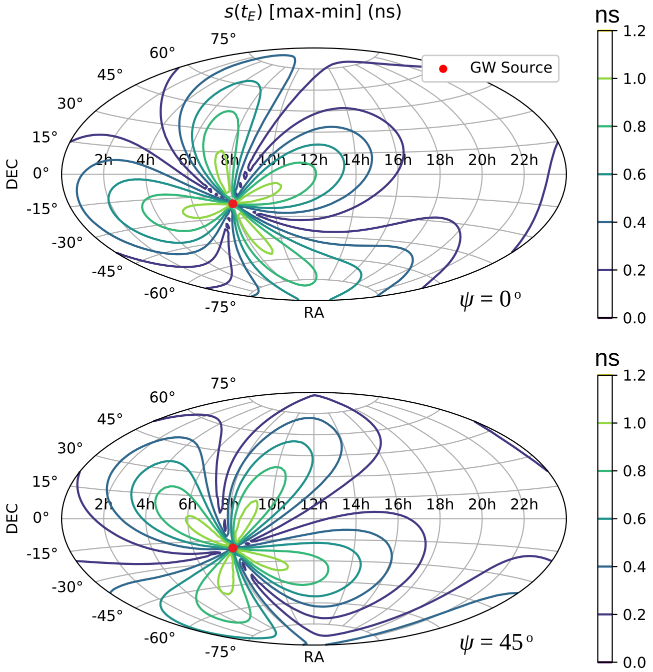

FIG. 6. Graphical display of the "strength" of the Earth term $s(t_E)$ as a function of pulsar's sky location. The two panels are for two specific values of the GW polarization angle and the rest of the parameters are identical to those employed in Fig. 4 with $P_b = 1.5$ yrs at $t_E = 0$. In these plots, the red dot represents the sky location of the GW source and the expected quadrupolar pattern is clearly visible. We rotate the bottom panel plot by 45° with respect to the top panel plot in accordance with the ψ values used.

the integration span as well as the number of TOAs when the number of TOAs is sufficiently large. This impressive feature may be contrasted with the fact that the execution time, when TOA numbers are small, is dominated by the one-time evaluation of various coefficients like κ, α and β.

The bottom panel of Fig. 7 compares the performance gain of our semianalytic method with respect to the usual approach of solving numerically Eqs. (17) by employing the ratio of execution times ($t^{\rm exec}_{\rm num}/t^{\rm exec}_{\rm anl}$). The associated plots reveal that this ratio increases substantially as one increases the integration span, especially for low $N_{\rm TOA}$ values. However, the ratio eventually decreases and essentially converges to a value close to 5 when $N_{\rm TOA}$ is a large number. This behavior is expected, since a numerical *ODE solver* is required to compute the right hand side of Eqs. (17) at many points between the TOAs where the solutions are required while evolving the binary over time. In contrast, our semianalytic approach *only computes* the solutions at the required TOAs. However, as the number of TOAs within an integration span increases, the number of intermediate points required by the numerical solver decreases too. This leads to the behavior displayed in the bottom panel of Fig. 7, and we infer that the semianalytic solution usually outperforms the numerical one.

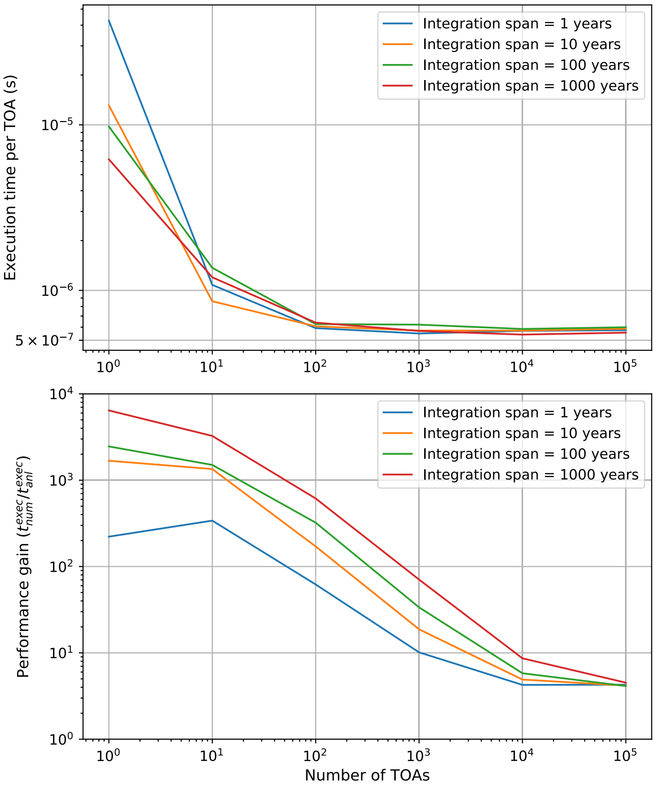

FIG. 7. Plots that compare execution times associated with the evolution of an eccentric binary using two approaches. The numerical approach (*num*) solves the set of four differential equations, given by Eqs. (17), by employing the gsl_odeiv2_step_rkf45 adaptive integration method of the GNU Scientific Library (GSL). The special functions, required by our analytic approach, are also evaluated with the help of GSL. We consider equal mass BH binaries with $M = 10^9\,M_\odot$, $P_{b0} = 1.5$ years, $e_{t0} = 0.5$, and let $l_0 = \gamma_0 = 0$. These computations were performed in C++ in an Intel Core i7 machine using a single core. These plots reveal that our semianalytic approach is more efficient that the regular numerical approach.

Figure 8 shows the time taken to compute the PTA signal $R(t)$ per TOA ($t^{\rm exec}_{\rm signal}/N_{\rm TOA}$) as a function of $N_{\rm TOA}$ for different integration spans. Once again, we see that the execution time is dominated by the one-time computations when $N_{\rm TOA}$ is small, but is independent of $N_{\rm TOA}$ when $N_{\rm TOA}$ is large. A comparison of Fig. 8 with the top panel of Fig. 7 reveals that the execution time of computing $R(t)$ is dominated by the cost of numerically integrating $h(t)$ to get $R(t)$.

Clearly, it is desirable to provide appropriate checks to verify the correctness of our detailed prescription for computing pulsar timing residuals, induced by relativistic eccentric binaries as it involves many numerical ingredients and detailed and lengthy analytic expressions. This is pursued in the next section where we provide a fully analytic way to compute $+/\times$ residuals for nonspinning BH binaries moving in PN-accurate *moderately eccentric* orbits.

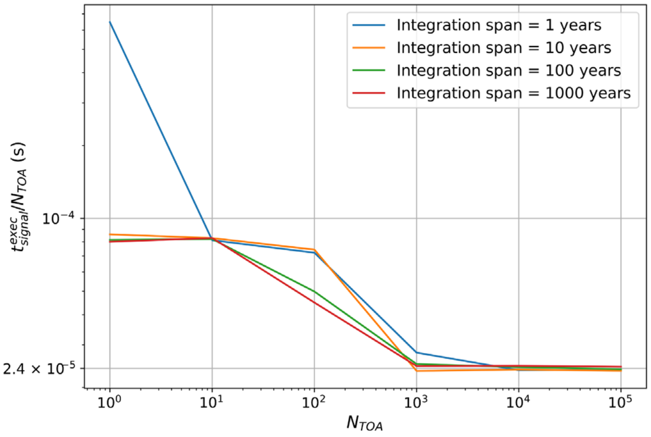

FIG. 8. The execution time per TOA for computing $R(t)$. For small N_{TOA} the execution time is dominated by one-time computations whereas for large N_{TOA} it is essentially independent of N_{TOA}. A comparison with the top panel of Fig. 7 also reveals that the execution time is dominated by the numerical integration of $h(t)$ to compute $R(t)$.

III. FULLY ANALYTIC $+/\times$ RESIDUALS FOR BINARIES IN POST-KEPLERIAN SMALL-ECCENTRICITY ORBITS

This section provides a fully analytic way of computing pulsar timing residuals due to BH binaries moving in quasi-Keplerian orbits of moderate eccentricities. This effort invokes explicit analytic expressions for $h^{Q}_{+,\times}(t)$ that are associated with nonspinning compact binaries moving in conservative 3PN-accurate small eccentricity orbits, derived in Ref. [45]. The main motivation, as noted earlier, is to provide a powerful check on the results, originating from our semianalytic approach, for computing $s_{+,\times}(t)$ associated with quasi-Keplerian orbits of arbitrary eccentricities. The present section is also influenced by Ref. [47] that provided explicit analytic expressions for the quadrupolar order $+$, $\times$ residuals from BH binaries in Newtonian eccentric orbits.

The effort, detailed in Ref. [47], employs various results from the Fourier analysis of the classical Kepler equation in terms of the Bessel functions, available in Ref. [60] and apply them in the quadrupolar order $h^{Q}_{+,\times}$ expressions, given by Eqs. (7) [61]. The resulting fully analytic Newtonian GW polarization states may be symbolically written as [47]

$$h_+(t) = \sum_{p=0}^{\infty} (a_p^+ \cos(pl)\cos(2\omega) + b_p^+ \sin(pl)\sin(2\omega) + c_p^+ \cos(pl)), \tag{38a}$$

$$h_\times(t) = \sum_{p=0}^{\infty} (a_p^\times \cos(pl)\sin(2\omega) + b_p^\times \sin(pl)\cos(2\omega)), \tag{38b}$$

where the coefficients $a_p^{+,\times}$, $b_p^{+,\times}$ and c_p^+ contain trigonometric functions of the orbital inclination i, while the orbital eccentricity e_t enters in terms of Bessel functions of the first kind [62]. Recall that ω provides the argument of periapsis, which remains a constant for Newtonian orbits. This ensures that such Newtonian compact binaries emit GWs at frequencies that are integer harmonics of n. It is also possible to incorporate in an *ad hoc* manner the linear-in-time evolution of ω to the above Newtonian order $h_{+,\times}$ expressions [63,64]. Employing the above Newtonian order expressions for the two GW polarizations states, Ref. [47] computed analytically the $+/\times$ residuals which may be written symbolically as

$$s_+(t) = \sum_{p=0}^{\infty} \frac{1}{np} (a_p^+ \sin(pl)\cos(2\omega) - b_p^+ \cos(pl)\sin(2\omega) + c_p^+ \sin(pl)), \tag{39a}$$

$$s_\times(t) = \sum_{p=0}^{\infty} \frac{1}{np} (a_p^\times \sin(pl)\sin(2\omega) - b_p^\times \cos(pl)\cos(2\omega)). \tag{39b}$$

The explicit form of these coefficients may be easily extracted with the help of Eqs. (21) and (22) of Ref. [47]. In what follows, we provide a fully post-Newtonian accurate version of these results.

Recall that fully analytic $h^{Q}_{+,\times}(l)$ expressions for compact binaries moving in conservative 3PN-accurate quasi-Keplerian small eccentric orbits were derived in Ref. [45]. This derivation employed Eqs. (7) for $h^{Q}_{+,\times}$ and an analytic treatment of the PN-accurate Kepler equation. The detailed analysis of Ref. [45] provided PN-accurate expressions for both eccentric and true anomalies in terms of infinite series expressions involving l and e_t. We write symbolically the resulting quadrupolar order $h_{+,\times}(l)$ expressions as

$$\begin{aligned} h_{+,\times}(t) = \sum_{p=0}^{\infty}\sum_{q=0}^{\infty} \{ & a_{p,q}^{+,\times} \cos(pl)\cos(q\lambda) \\ & + b_{p,q}^{+,\times} \sin(pl)\cos(q\lambda) \\ & + c_{p,q}^{+,\times} \cos(pl)\sin(q\lambda) \\ & + d_{p,q}^{+,\times} \sin(pl)\sin(q\lambda)\}, \end{aligned} \tag{40}$$

where we have defined $\lambda = l + \gamma$ [45]. A straightforward integration of the above expression leads to

$$\begin{aligned} s_{+,\times}(t) = \frac{1}{n} {\sum_{p,q=0}^{\infty}}' \{ & A_{p,q}^{+,\times} \cos(pl)\cos(q\lambda) \\ & + B_{p,q}^{+,\times} \sin(pl)\cos(q\lambda) \\ & + C_{p,q}^{+,\times} \cos(pl)\sin(q\lambda) \\ & + D_{p,q}^{+,\times} \sin(pl)\sin(q\lambda)\}, \end{aligned} \tag{41}$$

where we have ignored the effects of GW emission while performing various integrations. This is justified as the radiation reaction timescale is substantially larger than the orbital and advance of periapsis timescales. Further, the primed sum excludes the $p = q = 0$ term in the above expressions. These multi-index A, B, C, D coefficients involve x, η, trigonometric functions of i, and e_t contributions via infinite series of Bessel functions. They may be expressed as

$$A_{p,q}^{+,\times} = \frac{-pb_{p,q}^{+,\times} + (1+k)qc_{p,q}^{+,\times}}{p^2 - (1+k)^2 q^2}, \tag{42a}$$

$$B_{p,q}^{+,\times} = \frac{pa_{p,q}^{+,\times} + (1+k)qd_{p,q}^{+,\times}}{p^2 - (1+k)^2 q^2}, \tag{42b}$$

$$C_{p,q}^{+,\times} = \frac{-pd_{p,q}^{+,\times} - (1+k)qa_{p,q}^{+,\times}}{p^2 - (1+k)^2 q^2}, \tag{42c}$$

$$D_{p,q}^{+,\times} = \frac{pc_{p,q}^{+,\times} - (1+k)qb_{p,q}^{+,\times}}{p^2 - (1+k)^2 q^2}. \tag{42d}$$

Clearly, it is neither advisable nor feasible to evaluate these coefficients for arbitrarily high p and q values to high precision. This is because the underlying Bessel function evaluations are computationally very expensive. However, it is straightforward to obtain Taylor expansions of these coefficients around $e_t = 0$. The resulting expansions, accurate up to some $\mathcal{O}(e_t^m)$, ensure that the Fourier coefficients beyond a certain $p_{\max}$ and $q_{\max}$ vanish for any given m. This is essentially due to the following property of the Bessel functions of the first kind

$$\lim_{x\to 0} \mathrm{J}_m(x) \sim \mathcal{O}(x^m).$$

Unfortunately, both the Fourier series, given by Eqs. (42) and the associated power series expansions for the involved A, B, C, D coefficients converge slowly for moderately large e_t values. This might signal the breaking down of the approximation and may be associated with the celebrated Laplace limit [65]. Detailed comparisons of various Bessel function contributions, computed numerically and analytically, reveal that such an expansion accurate up to $\mathcal{O}(e_t^8)$ can be used to compute timing residuals for eccentricities less than 0.3. In what follows, we display the explicit expressions for the quadrupolar order $h_+^Q(l)$ that includes all the eccentricity corrections up to $\mathcal{O}(e_t^4)$, and the associated + residual:

$$\begin{aligned} h_+^Q = \mathcal{H}_0 \Bigg[& \left(e_t s_i^2 - \frac{1}{8} e_t^3 s_i^2\right)\cos(l) + \left(e_t^2 s_i^2 - \frac{1}{3} e_t^4 s_i^2\right)\cos(2l) \\ & + \left(-\frac{1}{8} 23 e_t^4 c_i^2 + 5 e_t^2 c_i^2 - 2 c_i^2 - \frac{23 e_t^4}{8} + 5 e_t^2 - 2\right)\cos(2\lambda) \\ & + \left(\frac{1}{8} e_t^4 c_i^2 + \frac{e_t^4}{8}\right)\cos(4l - 2\lambda) + \left(-\frac{1}{4} 81 e_t^4 c_i^2 - \frac{81 e_t^4}{4}\right)\cos(2\lambda + 4l) \\ & + \left(\frac{171}{16} e_t^3 c_i^2 - \frac{9 e_t c_i^2}{2} + \frac{171 e_t^3}{16} - \frac{9 e_t}{2}\right)\cos(2\lambda + l) + \left(\frac{7}{48} e_t^3 c_i^2 + \frac{7 e_t^3}{48}\right)\cos(3l - 2\lambda) \\ & + \left(-\frac{1}{48} 625 e_t^3 c_i^2 - \frac{625 e_t^3}{48}\right)\cos(2\lambda + 3l) + (20 e_t^4 c_i^2 - 8 e_t^2 c_i^2 + 20 e_t^4 - 8 e_t^2)\cos(2\lambda + 2l) \\ & + \left(-\frac{1}{16} 13 e_t^3 c_i^2 + \frac{3 e_t c_i^2}{2} - \frac{13 e_t^3}{16} + \frac{3 e_t}{2}\right)\cos(l - 2\lambda) + \frac{9}{8} e_t^3 s_i^2 \cos(3l) + \frac{4}{3} e_t^4 s_i^2 \cos(4l) \Bigg], \end{aligned} \tag{43a}$$

$$\begin{aligned} s_+^Q = \frac{\mathcal{H}_0}{n} \Bigg[& \left(e_t s_i^2 - \frac{1}{8} e_t^3 s_i^2\right)\sin(l) + \left(\frac{1}{2} e_t^2 s_i^2 - \frac{1}{6} e_t^4 s_i^2\right)\sin(2l) \\ & + \left(-\frac{1}{16} 23 e_t^4 c_i^2 + \frac{5}{2} e_t^2 c_i^2 - c_i^2 - \frac{23 e_t^4}{16} + \frac{5 e_t^2}{2} - 1\right)\sin(2\lambda) \\ & + \left(\frac{13}{16} e_t^3 c_i^2 - \frac{3 e_t c_i^2}{2} + \frac{13 e_t^3}{16} - \frac{3 e_t}{2}\right)\sin(l - 2\lambda) + \left(\frac{57}{16} e_t^3 c_i^2 - \frac{3 e_t c_i^2}{2} + \frac{57 e_t^3}{16} - \frac{3 e_t}{2}\right)\sin(2\lambda + l) \\ & + \left(\frac{1}{16} e_t^4 c_i^2 + \frac{e_t^4}{16}\right)\sin(4l - 2\lambda) + \left(-\frac{1}{8} 27 e_t^4 c_i^2 - \frac{27 e_t^4}{8}\right)\sin(2\lambda + 4l) \\ & + \left(\frac{7}{48} e_t^3 c_i^2 + \frac{7 e_t^3}{48}\right)\sin(3l - 2\lambda) + \left(-\frac{1}{48} 125 e_t^3 c_i^2 - \frac{125 e_t^3}{48}\right)\sin(2\lambda + 3l) \\ & + (5 e_t^4 c_i^2 - 2 e_t^2 c_i^2 + 5 e_t^4 - 2 e_t^2)\sin(2\lambda + 2l) + \frac{1}{3} e_t^4 s_i^2 \sin(4l) + \frac{3}{8} e_t^3 s_i^2 \sin(3l) \Bigg], \end{aligned} \tag{43b}$$

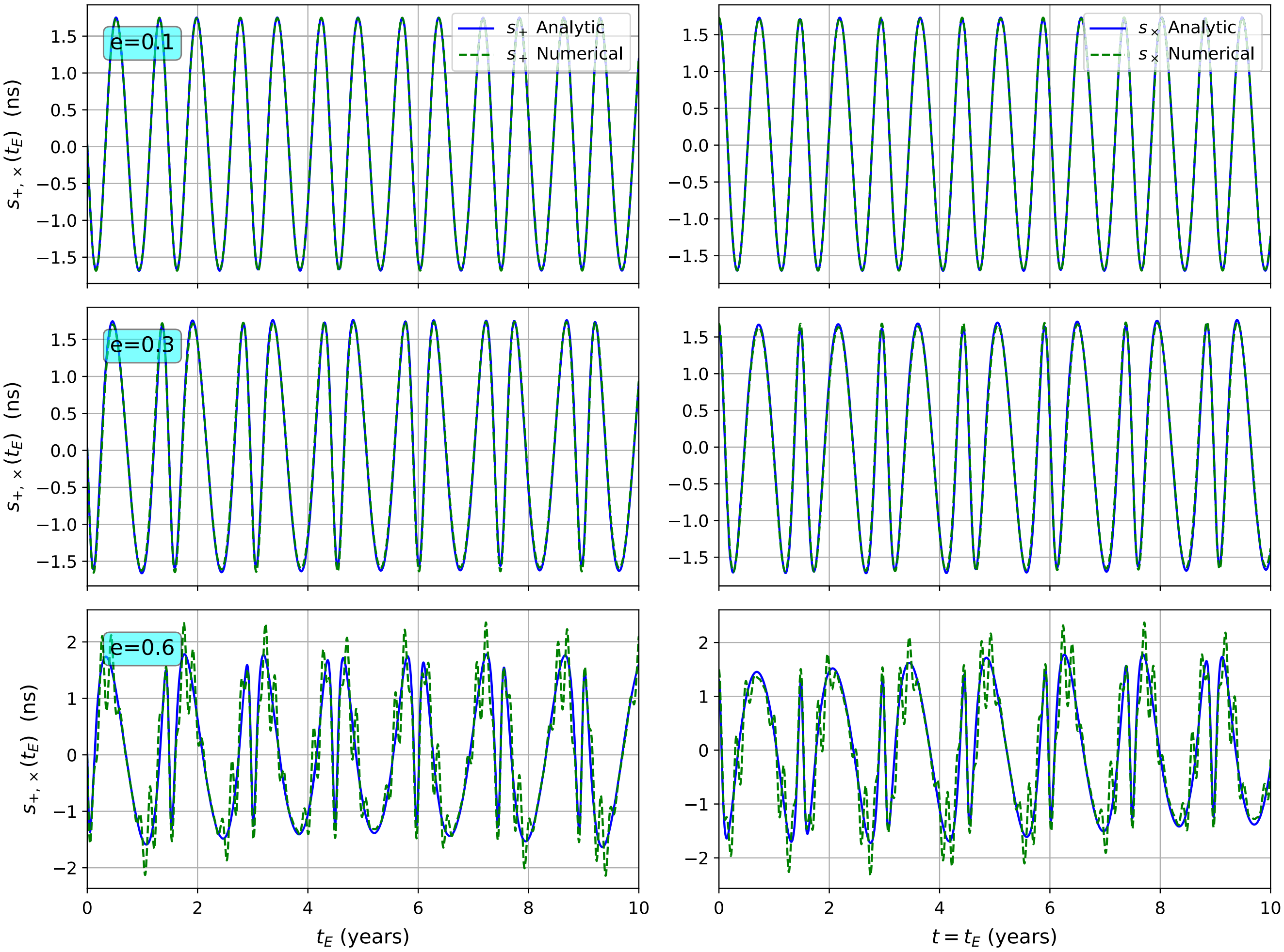

FIG. 9. We overlay $s_{+,\times}(t)$ plots for an equal mass binary with different eccentricities that arise from our fully analytic postcircular approximation and the earlier described semianalytic approach. The binary parameters are the same as in Fig. 5 with $P_b = 1.5$ yrs at $t_E = 0$ and the postcircular approximation includes all terms accurate up to $\mathcal{O}(e_t^8)$. We observe that the quality of the postcircular approximation degrades as the eccentricity increases, as expected.

where we have defined $\mathcal{H}_0 = \frac{GM\eta}{D_L c^2} x$. We note in passing that we have explicitly computed the quadrupolar order $h_{+,\times}(l)$ and its temporally evolving $+/\times$ residuals that include all the $\mathcal{O}(e_t^8)$ corrections. Additionally, these expressions were employed while making comparisons of our analytic and semianalytic approaches to compute $s_{+,\times}(t)$, displayed in Fig. 9.

We are now in a position to use these expressions to test our involved semianalytical approach to obtain $+/\times$ residuals valid for arbitrary eccentricities. In Fig. 9, we overlay plots of $s^{Q}_{+,\times}(t)$ that arise from the above mentioned analytic approach and our semianalytic approach while focusing only on the Earth term for three initial values of e_t. Additionally, we let the orbital elements and angles vary according to our improvised GW phasing approach, detailed in Sec. II C, in both the approaches. We observe excellent agreement between the two approaches for initial e_t values up to 0.3 and it is difficult to distinguish the dashed line plots in the first two panels. Therefore, these plots give us the confidence about the correctness of our semianalytic approach to obtain $R(t)$ for BH binaries inspiraling along relativistic eccentric orbits. However, our analytic postcircular approach becomes progressively worse for a larger initial e value as evident from the bottom panel plots. We quantify the deviation between our semianalytic and fully analytic temporally evolving plus/cross residuals with the help of the following normalized integrated error defined as

$$\varepsilon(e_0) = \frac{\sum_i [(s_+^{\mathrm{num}}(t_i) - s_+^{\mathrm{anl}}(t_i))^2 + (s_\times^{\mathrm{num}}(t_i) - s_\times^{\mathrm{anl}}(t_i))^2]}{\sum_i [(s_+^{\mathrm{num}}(t_i))^2 + (s_\times^{\mathrm{num}}(t_i))^2]}. \tag{44}$$

In Fig. 10, we plot ε as a function of initial orbital eccentricity for different combinations of P_b, M and η. This plot reinforces our conclusion that our postcircular

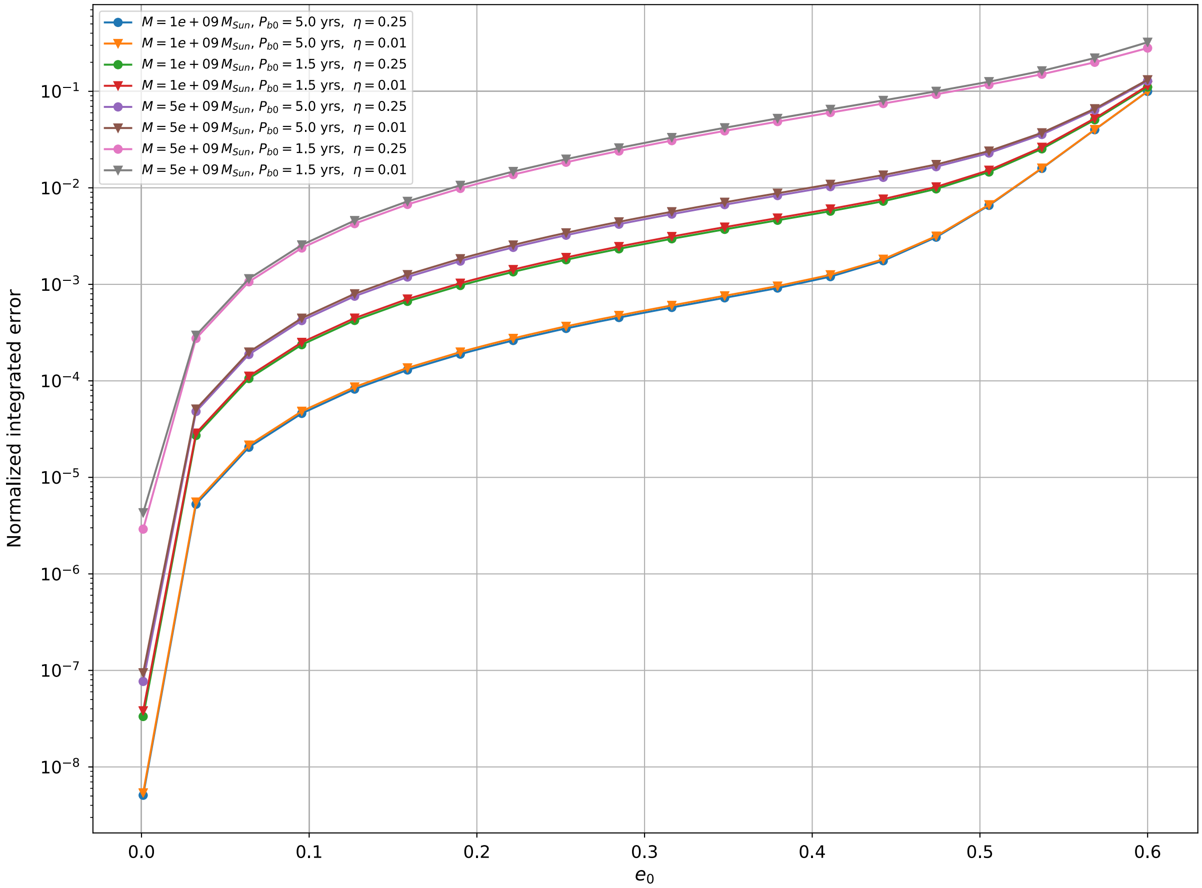

FIG. 10. The normalized integrated error in the postcircular approximation as a function of the initial eccentricity for different combinations of P_b, M and η. Rest of the binary parameters are identical to those used in Fig. 9 and the normalized integrated error is defined using Eq. (44). Clearly, the approximation gets progressively worse as we increase initial eccentricity values. In addition, the accuracy of the approximation decreases with shorter orbital periods and with higher masses. However, the error is only weakly dependent on the mass ratio.

approximation shows good agreement with the numerical approach for $e < 0.3$ values. The accuracy of the postcircular approximation is also seen to degrade for shorter orbital periods and for higher masses (i.e., more relativistic). This behavior is reflective of the truncation error arising from the analytic Fourier series solution for the 3PN Kepler equation and it is discussed in detail in Ref. [45]. We note in passing that substantial differences between our two approaches for higher e_0 values may be related to the Laplace limit associated with the analytic solution to the classical Kepler equation.

IV. SUMMARY AND DISCUSSIONS

The present work provides a computationally efficient way to compute pulsar timing residuals induced by GWs from isolated massive BH binaries inspiraling along general relativistic eccentric orbits. The use of an improvised version of the GW phasing approach, detailed in Refs. [42,43], and the PN-accurate quasi-Keplerian parametrization allowed us to model binary BH orbits that inspiral due to the emission of quadrupolar GWs along 3PN-accurate eccentric orbits in an essentially analytic manner. This leads to analytic solutions for the mean motion n, mean anomaly l and the periapsis angle γ in terms of PN-accurate time eccentricity e_t as well as system-dependent constants and initial conditions. This is augmented by using a computationally efficient way to obtain certain scaled temporal evolution for e_t imposed by the quadrupolar order GW emission. These inputs allowed us to obtain the quadrupolar order temporally evolving GW polarization states, the associated $+/\times$ residuals and the resulting pulsar timing residuals $R(t)$ due to PN-accurate eccentric inspirals in a computationally inexpensive way. Additionally, we provided a fully analytic prescription to compute analytic $+/\times$ residuals due to BH binaries moving in 3PN-accurate small eccentricity orbits. The excellent agreement between these two approaches provided a powerful check for our very involved semianalytic approach, appropriate for arbitrary orbital eccentricities.

We have implemented our prescription to compute pulsar timing residuals induced by GWs from arbitrary eccentricity BH binaries, developed in Sec. II, as well as our fully analytic prescription to compute timing residuals for low-eccentricity binaries developed in Sec. III, in a C++ package called GWecc [66]. We are working to integrate these codes into the popular PTA-relevant packages like TEMPO2 and Enterprise. This should allow us to constrain the presence of isolated eccentric BH binaries in the latest Parkes Pulsar Timing Array (PPTA) dataset [67]. Further, efforts are ongoing to tackle the IPTA DR2 and Nanograv 12.5 year datasets by employing the present prescription [68]. Clearly, it will be interesting to explore the effects of higher order GW radiation reaction effects in the equations for $\dot{n}$ and $\dot{e}_t$. It is reasonable to expect that such contributions will be more relevant for the pulsar contributions to $R(t)$ due to the lengthy temporal separation between the Earth and the Pulsar epochs and this is currently under investigation. Moreover, we are also pursuing detailed investigations on the implementation of certain Generalized Likelihood Ratio Tests for the PTA detection of eccentric precessing BH binaries, influenced by Ref. [69].

It turns out that the spin-orbit coupling can influence the nature of PTA signals from nonspinning massive BH binaries as this contribution enters the dynamics at the 1.5PN order. Therefore, we are extending the present approach by incorporating the spin effects, influenced by Refs. [70,71]. This effort relies on the availability of a Keplerian-type parametric solution for the dynamics of compact binaries that incorporates the effects of dominant order spin-orbit interactions [72].

ACKNOWLEDGMENTS

We thank Yannick Boetzel for helpful discussions and providing his Mathematica notebook, Lankeswar Dey and Xingjiang Zhu for helpful discussions, and Belinda Cheeseboro for testing and providing valuable suggestions regarding GWecc. A. S. wishes to thank the hospitality of CSIRO Astronomy and Space Sciences, ARC Centre of Excellence for Gravitational Wave Discovery (OzGrav) and Monash University. A. S. was partially supported by CSIRO and the Sarojini Damodaran Fellowship during the course of the collaboration. A. S. and A. G. acknowledge support of the Department of Atomic Energy, Government of India, under Project No. 12-R&D-TFR-5.02-0200. S. R. T. acknowledges support from the NANOGrav project, which is supported by the National Science Foundation (NSF) Physics Frontier Center Grant No. 1430284.

APPENDIX A: HIGHER ORDER PN CORRECTIONS TO $\gamma(t)$

This Appendix details our approach to integrate 3PN-accurate expression for $d\gamma/dt$ which may be written symbolically as

$$\frac{d\gamma}{dt} = (k_1 + k_2 + k_3)n. \tag{A1}$$

Recall that we have tackled the 1PN version of above equation, namely $d\gamma/dt = k_1 n$ in subsection II C. This Appendix extends such a solution while incorporating 2PN and 3PN contributions to the rate of periapsis advance. The fact that this rate is independent of γ allows us to express our Eq. (A1) as

$$\frac{d\gamma_j}{dt} = k_j n, \tag{A2}$$

where

$$\gamma = \sum_{j=1}^{\infty} \gamma_j. \tag{A3}$$

At the 2PN order, we have [43]

$$k_2 = \left(\frac{GMn}{c^3}\right)^{4/3} \frac{((51 - 26\eta)e_t^2 - 28\eta + 78)}{4(1 - e_t^2)^2}. \tag{A4}$$

This leads to

$$\frac{d\gamma_2}{dt} = \frac{1}{4}\left(\frac{GMn}{c^3}\right)^{4/3} n \frac{((51 - 26\eta)e_t^2 - 28\eta + 78)}{(1 - e_t^2)^2}. \tag{A5}$$

Introducing τ variable with the help of Eqs. (19), (20b) and (21) allows us to write

$$\frac{d\gamma_2}{d\tau} = -\beta_2 \frac{(1 - e_t^2)^{\frac{3}{2}}}{e_t^{\frac{42}{19}}} \frac{((51 - 26\eta)e_t^2 - 28\eta + 78)}{(304 + 121e_t^2)^{\frac{3045}{2299}}}, \tag{A6}$$

where

$$\beta_2 = \frac{15}{4}\left(\frac{GM_{\mathrm{ch}}n_0}{c^3}\right)^{-5/3}\left(\frac{GMn_0}{c^3}\right)^{4/3} \times \frac{\sqrt{1 - e_{t0}^2}}{e_{t0}^{6/19}(121e_{t0}^2 + 304)^{435/2299}}. \tag{A7}$$

We now introduce $\bar{\gamma}_2 = \Gamma_{20} - \frac{\gamma_2}{\beta_2}$, where Γ_{20} is a constant. The above equation then becomes

$$\frac{d\bar{\gamma}_2}{d\tau} = \frac{(1 - e_t^2)^{\frac{3}{2}}}{e_t^{\frac{42}{19}}} \frac{((51 - 26\eta)e_t^2 - 28\eta + 78)}{(304 + 121e_t^2)^{\frac{3045}{2299}}}. \tag{A8}$$

We define γ_2 such that $\gamma_2(\tau_0) = 0$. This allows us to fix Γ_{20} to be $\Gamma_{20} = \bar{\gamma}_2(\tau_0)$. We move on to obtain $d\bar{\gamma}_2/de_t$ by dividing Eq. (A8) by Eq. (21), which gives us

$$\frac{d\bar{\gamma}_2}{de_t} = \frac{e_t^2(51 - 26\eta) - 28\eta + 78}{e_t^{13/19}(121e_t^2 + 304)^{\frac{1864}{2299}}}. \tag{A9}$$

This can be integrated to obtain

$$\bar{\gamma}_2(e_t) = \frac{e_t^{6/19}}{336}\left(4(121e_t^2+304)^{\frac{435}{2299}}(51-26\eta) + 3\times 2^{\frac{1740}{2299}}19^{\frac{435}{2299}}(2\eta+23)\,{}_2\mathrm{F}_1\left(\frac{3}{19},\frac{1864}{2299};\frac{22}{19};\frac{-121e_t^2}{304}\right)\right). \tag{A10}$$

Few comments are in order at this point. It should be obvious that we are splitting the GW emission-induced temporal evolution for γ in parts. This is mainly because we assume that the GW emission is fully prescribed by Eqs. (17). And, it explains why we divided $d\bar{\gamma}_1/d\tau$ and $d\bar{\gamma}_2/d\tau$ equations the same equation, namely Eq. (21) for $de_t/d\tau$. In other words, the above split and our division of the resulting equations by Eq. (21) is rather inconsistent if there are higher order contributions to GW emission.

With the help of these considerations, we move on to write 3PN contributions to $d\gamma/dt$ as $d\gamma_3/dt = k_3 n$ where

$$\begin{aligned}k_3 = {} & \left(\frac{GMn}{c^3}\right)^2 \frac{1}{128(1-e_t^2)^3}\Big(18240 - 25376\eta + 492\pi^2\eta + 896\eta^2 + (28128 - 27840\eta + 123\pi^2\eta + 5120\eta^2)e_t^2 \\ & + (2496 - 1760\eta + 1040\eta^2)e_t^4 + (1920 - 768\eta + (3840 - 1536\eta)e_t^2)\sqrt{1-e_t^2}\Big).\end{aligned} \tag{A11}$$

Following the steps that we pursued at the 2PN order leads us to

$$\begin{aligned}\frac{d\bar{\gamma}_3}{de_t} = {} & \frac{1}{e_t^{\frac{25}{19}}(121e_t^2+304)^{\frac{2734}{2299}}}\Big(18240 - 25376\eta + 492\pi^2\eta + 896\eta^2 + (28128 - 27840\eta + 123\pi^2\eta + 5120\eta^2)e_t^2 \\ & + (2496 - 1760\eta + 1040\eta^2)e_t^4 + (1920 - 768\eta + (3840 - 1536\eta)e_t^2)\sqrt{1-e_t^2}\Big),\end{aligned} \tag{A12}$$

where we have defined $\bar{\gamma}_3 = \Gamma_{30} - \frac{\gamma_3}{\beta_3}$, $\Gamma_{30} = \bar{\gamma}_3(\tau_0)$. Further, the coefficient β_3 is given by

$$\beta_3 = \frac{15}{128}\left(\frac{GM_{\mathrm{ch}}n_0}{c^3}\right)^{-5/3}\left(\frac{GMn_0}{c^3}\right)^2 \frac{e_{t0}^{6/19}(121e_{t0}^2+304)^{435/2299}}{\sqrt{1-e_{t0}^2}}. \tag{A13}$$

The equation for $\bar{\gamma}_3$ can be solved to get

$$\begin{aligned}\bar{\gamma}_3(e_t) = {} & -\frac{2957312\sqrt{1-e_t^2}(2\eta-5)\,\mathrm{F}_1^{\mathrm{A}}(\frac{-3}{19};\frac{-1}{2},\frac{2734}{2299};\frac{16}{19};e_t^2,\frac{-121e_t^2}{304})}{e_t^{6/19}(121e_t^2+304)^{\frac{2734}{2299}}} \\ & \times\Bigg[e_t^2\left(1444\,\mathrm{F}_1^{\mathrm{A}}\left(\frac{16}{19};\frac{1}{2},\frac{2734}{2299};\frac{35}{19};e_t^2,\frac{-121e_t^2}{304}\right) + 1367\,\mathrm{F}_1^{\mathrm{A}}\left(\frac{16}{19};\frac{-1}{2},\frac{5033}{2299};\frac{35}{19};e_t^2,\frac{-121e_t^2}{304}\right)\right) \\ & - 2432\,\mathrm{F}_1^{\mathrm{A}}\left(\frac{-3}{19};\frac{-1}{2},\frac{2734}{2299};\frac{16}{19};e_t^2,\frac{-121e_t^2}{304}\right)\Bigg]^{-1} \\ & + \frac{2425920e_t^{32/19}\sqrt{1-e_t^2}(2\eta-5)\,\mathrm{F}_1^{\mathrm{A}}(\frac{16}{19};\frac{-1}{2},\frac{2734}{2299};\frac{35}{19};e_t^2,\frac{-121e_t^2}{304})}{(121e_t^2+304)^{2734/2299}} \\ & \times\Bigg[e_t^2\left(1444\,\mathrm{F}_1^{\mathrm{A}}\left(\frac{35}{19};\frac{1}{2},\frac{2734}{2299};\frac{54}{19};e_t^2,\frac{-121e_t^2}{304}\right) + 1367\,\mathrm{F}_1^{\mathrm{A}}\left(\frac{35}{19};\frac{-1}{2},\frac{5033}{2299};\frac{54}{19};e_t^2,\frac{-121e_t^2}{304}\right)\right) \\ & - 5320\,\mathrm{F}_1^{\mathrm{A}}\left(\frac{16}{19};\frac{-1}{2},\frac{2734}{2299};\frac{35}{19};e_t^2,\frac{-121e_t^2}{304}\right)\Bigg]^{-1} + \frac{1}{53760\times 2^{1740/2299}19^{435/2299}e_t^{6/19}} \\ & \times\Bigg[105e_t^2(5120\eta^2 + 3(41\pi^2-9280)\eta + 28128)\,{}_2\mathrm{F}_1\left(\frac{16}{19},\frac{2734}{2299};\frac{35}{19};\frac{-121e_t^2}{304}\right) \\ & - 2240(224\eta^2 + (123\pi^2-6344)\eta + 4560)\,{}_2\mathrm{F}_1\left(\frac{-3}{19},\frac{2734}{2299};\frac{16}{19};\frac{-121e_t^2}{304}\right) \\ & + 768e_t^4(65\eta^2 - 110\eta + 156)\,{}_2\mathrm{F}_1\left(\frac{2734}{2299},\frac{35}{19};\frac{54}{19};\frac{-121e_t^2}{304}\right)\Bigg].\end{aligned} \tag{A14}$$

Let us note again that, assuming the GW emission is fully characterised by our quadrupolar order equations, we write

$$\gamma(e_t) = \gamma_0 - \beta_1(\bar{\gamma}_1(e_t) - \bar{\gamma}_1(e_{t0})) - \beta_2(\bar{\gamma}_2(e_t) - \bar{\gamma}_2(e_{t0})) - \beta_3(\bar{\gamma}_3(e_t) - \bar{\gamma}_3(e_{t0})), \tag{A15}$$

as we strictly assume that the GW emission is fully characterized by our quadrupolar order equations.

APPENDIX B: REACTIVE EVOLUTION OF CIRCULAR ORBITS

This Appendix lists the circular limit of GW phasing equations, detailed in Sec. II C. A careful treatment is required as $\kappa \to 0$ for circular orbits. However, we may obtain $e_t \to 0$ limit of Eqs. (17) and it reads

$$\frac{dn}{dt} = \frac{96}{5}\left(\frac{GM_{\mathrm{ch}}n}{c^3}\right)^{\frac{5}{3}} n^2, \tag{B1a}$$

$$\frac{de_t}{dt} = 0, \tag{B1b}$$

$$\frac{dl}{dt} = n, \tag{B1c}$$

$$\frac{d\gamma}{dt} = 3\left(\frac{GMn}{c^3}\right)^{2/3} n + \frac{(78-28\eta)}{4}\left(\frac{GMn}{c^3}\right)^{4/3} n + \frac{(896\eta^2 + 492\pi^2\eta - 26144\eta + 20160)}{128}\left(\frac{GMn}{c^3}\right)^2 n, \tag{B1d}$$

where we have included the 2PN and 3PN contributions to $d\gamma/dt$, using the circular limits of Eqs. (A4) and (A11). Since the periapsis is not well defined for a circular orbit, it is advisable to define the angular variable $\lambda = l + \gamma$ and the sidereal orbital frequency $n_s = (1+k)n$. It is straightforward to see that, in terms of λ and n_s, the orbital evolution can be written as

$$\frac{dn_s}{dt} = \frac{96}{5}\left(\frac{GM_{\mathrm{ch}}n_s}{c^3}\right)^{\frac{5}{3}} n_s^2, \tag{B2a}$$

$$\frac{d\lambda}{dt} = n_s, \tag{B2b}$$

where we have restricted the reactive evolution to the leading order in the PN expansion.

These equations lead to the following analytic expressions for $n_s(t)$ and $\lambda(t)$:

$$n_s(t) = \frac{n_{s0}}{(1 - \frac{256}{5}(\frac{GM_{\mathrm{ch}}n_{s0}}{c^3})^{\frac{5}{3}} n_{s0}(t-t_0))^{3/8}}, \tag{B3a}$$

$$\lambda(t) = \lambda_0 + \frac{1}{32}\left(\frac{GM_{\mathrm{ch}}n_{s0}}{c^3}\right)^{-\frac{5}{3}}\left(1 - \left(\frac{n_{s0}}{n_s}\right)^{5/3}\right), \tag{B3b}$$

where n_{s0} and λ_0 are the values of these variables at some initial epoch $t = t_0$. The orbital eccentricity does not vary in time and its value is chosen to be zero.

The GW emission-induced merger time is obtained by demanding that $n \to \infty$ and this allows us to write

$$t_{\mathrm{merg}} = t_0 + \frac{5}{256 n_0}\left(\frac{GM_{\mathrm{ch}}n_0}{c^3}\right)^{-\frac{5}{3}}. \tag{B4}$$

We have verified that our eccentric version of the merger time, given by Eq. (24), reduces to Eq. (B4) in the circular limit.

[1] L. Z. Kelley, L. Blecha, L. Hernquist, A. Sesana, and S. R. Taylor, Mon. Not. R. Astron. Soc. **471**, 4508 (2017).

[2] LIGO Scientific Collaboration and Virgo Collaboration, Phys. Rev. X **9**, 031040 (2019).

[3] R. S. Foster and D. C. Backer, Astrophys. J. **361**, 300 (1990).

[4] A. N. Lommen, Rep. Prog. Phys. **78**, 124901 (2015).

[5] S. Detweiler, Astrophys. J. **234**, 1100 (1979).

[6] G. Hobbs, Classical Quantum Gravity **30**, 224007 (2013).

[7] M. Kramer and D. J. Champion, Classical Quantum Gravity **30**, 224009 (2013).

[8] M. A. McLaughlin, Classical Quantum Gravity **30**, 224008 (2013).

[9] A. Brazier, S. Chatterjee, T. Cohen, J. M. Cordes, M. E. DeCesar, P. B. Demorest, J. S. Hazboun, M. T. Lam, R. S. Lynch, M. A. McLaughlin, S. M. Ransom, X. Siemens, S. R. Taylor, and S. J. Vigeland, arXiv:1908.05356.

[10] B. C. Joshi, P. Arumugasamy, M. Bagchi, D. Bandyopadhyay, A. Basu, N. D. Batra, S. Bethapudi, A. Choudhary, K. De, L. Dey, A. Gopakumar, Y. Gupta, M. A. Krishnakumar, Y. Maan, P. K. Manoharan, A. Naidu, R. Nandi, D. Pathak, M. Surnis, and A. Susobhanan, J. Astrophys. Astron. **39**, 51 (2018).

[11] M. Bailes *et al.*, Proc. Sci., MeerKAT2016 (**2018**) 011 [arXiv:1803.07424].

[12] K. J. Lee, Prospects of gravitational wave detection using pulsar timing array for chinese future telescopes, in *Frontiers in Radio Astronomy and FAST Early Sciences*

Symposium 2015, Astronomical Society of the Pacific Conference Series, Vol. 502, edited by L. Qain and D. Li (Astronomical Society of the Pacific (ASP), Orem, USA, 2016), p. 19, http://aspbooks.org/a/volumes/article_details/?paper_id=37688.
[13] G. Hobbs *et al.*, Classical Quantum Gravity **27**, 084013 (2010).
[14] J. P. W. Verbiest *et al.*, Mon. Not. R. Astron. Soc. **458**, 1267 (2016).
[15] B. B. P. Perera *et al.*, Mon. Not. R. Astron. Soc. **490**, 4666 (2019).
[16] G. Hobbs and S. Dai, Natl. Sci. Rev. **4**, 707 (2017).
[17] S. Burke-Spolaor, S. R. Taylor, M. Charisi, T. Dolch, J. S. Hazboun, A. M. Holgado, L. Z. Kelley, T. J. W. Lazio, D. R. Madison, N. McMann, C. M. F. Mingarelli, A. Rasskazov, X. Siemens, J. J. Simon, and T. L. Smith, Astron. Astrophys. Rev. **27**, 5 (2019).
[18] P. A. Rosado, A. Sesana, and J. Gair, Mon. Not. R. Astron. Soc. **451**, 2417 (2015).
[19] L. Z. Kelley, L. Blecha, L. Hernquist, A. Sesana, and S. R. Taylor, Mon. Not. R. Astron. Soc. **477**, 964 (2018).
[20] Z. Arzoumanian *et al.* (NANOGrav Collaboration), Astrophys. J. **859**, 47 (2018).
[21] K. Aggarwal *et al.* (The NANOGrav Collaboration), Astrophys. J. **880**, 116 (2019).
[22] S. Babak *et al.*, Mon. Not. R. Astron. Soc. **455**, 1665 (2016).
[23] L. Lentati *et al.*, Mon. Not. R. Astron. Soc. **453**, 2576 (2015).
[24] Y. Feng, D. Li, Y.-R. Li, and J.-M. Wang, arXiv:1907.03460.
[25] N. K. Porayko *et al.* (PPTA Collaboration), Phys. Rev. D **98**, 102002 (2018).
[26] H. Middleton, S. Chen, W. Del Pozzo, A. Sesana, and A. Vecchio, Nat. Commun. **9**, 573 (2018).
[27] S. Chen, A. Sesana, and C. J. Conselice, Mon. Not. R. Astron. Soc. **488**, 401 (2019).
[28] S. Chen, H. Middleton, A. Sesana, W. Del Pozzo, and A. Vecchio, Mon. Not. R. Astron. Soc. **468**, 404 (2017).
[29] S. Taylor, S. Burke-Spolaor, P. T. Baker, M. Charisi, K. Islo, L. Z. Kelley, D. R. Madison, J. Simon, and S. Vigeland (Nanograv Collaboration), Bull. AAS **51**, 336 (2019).
[30] S. R. Taylor, J. Simon, and L. Sampson, Phys. Rev. Lett. **118**, 181102 (2017).
[31] P. J. Armitage and P. Natarajan, Astrophys. J. **634**, 921 (2005).
[32] J. Cuadra, P. J. Armitage, R. D. Alexander, and M. C. Begelman, Mon. Not. R. Astron. Soc. **393**, 1423 (2009).
[33] I. Berentzen, M. Preto, P. Berczik, D. Merritt, and R. Spurzem, Astrophys. J. **695**, 455 (2009).
[34] F. M. Khan, M. Preto, P. Berczik, I. Berentzen, A. Just, and R. Spurzem, Astrophys. J. **749**, 147 (2012).
[35] F. M. Khan, K. Holley-Bockelmann, P. Berczik, and A. Just, Astrophys. J. **773**, 100 (2013).
[36] C. Roedig and A. Sesana, J. Phys. Conf. Ser. **363**, 012035 (2012).
[37] R. T. Edwards, G. B. Hobbs, and R. N. Manchester, Mon. Not. R. Astron. Soc. **372**, 1549 (2006).
[38] G. B. Hobbs, R. T. Edwards, and R. N. Manchester, Mon. Not. R. Astron. Soc. **369**, 655 (2006).
[39] J. A. Ellis, S. R. Taylor, P. T. Baker, and M. Vallisneri, ENTERPRISE: Enhanced Numerical Toolbox Enabling a Robust PulsaR Inference SuitE (2019), https://ui.adsabs.harvard.edu/abs/2019ascl.soft12015E.
[40] L. Blanchet, Living Rev. Relativity **17**, 2 (2014).
[41] R.-M. Memmesheimer, A. Gopakumar, and G. Schäfer, Phys. Rev. D **70**, 104011 (2004).
[42] T. Damour, A. Gopakumar, and B. R. Iyer, Phys. Rev. D **70**, 064028 (2004).
[43] C. Königsdörffer and A. Gopakumar, Phys. Rev. D **73**, 124012 (2006).
[44] B. Moore, T. Robson, N. Loutrel, and N. Yunes, Classical Quantum Gravity **35**, 235006 (2018).
[45] Y. Boetzel, A. Susobhanan, A. Gopakumar, A. Klein, and P. Jetzer, Phys. Rev. D **96**, 044011 (2017).
[46] F. A. Jenet, A. Lommen, S. L. Larson, and L. Wen, Astrophys. J. **606**, 799 (2004).
[47] S. R. Taylor, E. A. Huerta, J. R. Gair, and S. T. McWilliams, Astrophys. J. **817**, 70 (2016).
[48] L. G. Book and É. E. Flanagan, Phys. Rev. D **83**, 024024 (2011).
[49] H. Wahlquist, Gen. Relativ. Gravit. **19**, 1101 (1987).
[50] K. J. Lee, N. Wex, M. Kramer, B. W. Stappers, C. G. Bassa, G. H. Janssen, R. Karuppusamy, and R. Smits, Mon. Not. R. Astron. Soc. **414**, 3251 (2011).
[51] T. Damour and N. Deruelle, Ann. Inst. Henri Poincaré Phys. Théor. **43**, 107 (1985).
[52] S. Tanay, M. Haney, and A. Gopakumar, Phys. Rev. D **93**, 064031 (2016).
[53] S. Tiwari, A. Gopakumar, M. Haney, and P. Hemantakumar, Phys. Rev. D **99**, 124008 (2019).
[54] S. Mikkola, Celest. Mech. **40**, 329 (1987).
[55] F. Colavecchia, G. Gasaneo, and J. Miraglia, Comput. Phys. Commun. **138**, 29 (2001).
[56] A. Królak, K. D. Kokkotas, and G. Schäfer, Phys. Rev. D **52**, 2089 (1995).
[57] M. Tessmer and A. Gopakumar, Mon. Not. R. Astron. Soc. **374**, 721 (2007).
[58] D. Zwillinger, *The Handbook of Integration*, 1st ed. (Jones and Bartlett, London, England, 1992).
[59] D. J. Reardon *et al.*, Mon. Not. R. Astron. Soc. **455**, 1751 (2016).
[60] P. Colwell, *Solving Kepler's Equation Over Three Centuries* (Willmann-Bell, Richmond, USA, 1993).
[61] P. C. Peters and J. Mathews, Phys. Rev. **131**, 435 (1963).
[62] C. Moreno-Garrido, E. Mediavilla, and J. Buitrago, Mon. Not. R. Astron. Soc. **274**, 115 (1995).
[63] N. Seto, Phys. Rev. Lett. **87**, 251101 (2001).
[64] L. Barack and C. Cutler, Phys. Rev. D **69**, 082005 (2004).
[65] G. N. Watson, *A Treatise on the Theory of Bessel Functions*, 2nd ed. (Cambridge University Press, Cambridge, England, 1966).
[66] `GWecc`, together with a Python wrapper, are available at https://github.com/abhisrkckl/GWecc.
[67] A. Susobhanan, X. J. Zhu, G. Hobbs, A. Gopakumar *et al.* (to be published).
[68] B. Cheeseboro, L. Dey, A. Susobhanan, S. Burke-Spolaor, A. Gopakumar *et al.* (to be published).

[69] Y. Wang, S. D. Mohanty, and F. A. Jenet, Astrophys. J. **815**, 125 (2015).

[70] C. M. F. Mingarelli, K. Grover, T. Sidery, R. J. E. Smith, and A. Vecchio, Phys. Rev. Lett. **109**, 081104 (2012).

[71] J.-W. Chen and Y. Zhang, Mon. Not. R. Astron. Soc. **481**, 2249 (2018).

[72] C. Königsdörffer and A. Gopakumar, Phys. Rev. D **71**, 024039 (2005).